9-2021

Verification and Validation of Radiation Protection Factors from Monte Carlo Simulations

William J. Erwin

VERIFICATION AND VALIDATION OF RADIATION PROTECTION FACTORS FROM MONTE CARLO SIMULATIONS

DISSERTATION

William J. Erwin, Major, USAR

AFIT-ENP-DS-21-S-027

DEPARTMENT OF THE AIR FORCE
AIR UNIVERSITY

AIR FORCE INSTITUTE OF TECHNOLOGY

Wright-Patterson Air Force Base, Ohio

AFIT-ENP-DS-21-S-027

VERIFICATION AND VALIDATION OF RADIATION PROTECTION FACTORS FROM MONTE CARLO SIMULATIONS

DISSERTATION

Presented to the Faculty

Department of Engineering Nuclear Physics

Graduate School of Engineering and Management

Air Force Institute of Technology

Air University

Air Education and Training Command

In Partial Fulfillment of the Requirements for the

Degree of Doctor of Philosophy

William J. Erwin, BE, MS

Major, USAR

December 2021

AFIT-ENP-DS-21-S-027

VERIFICATION AND VALIDATION OF RADIATION PROTECTION FACTORS FROM MONTE CARLO SIMULATIONS

DISSERTATION

William J. Erwin, BE, MS

Major, USAR

Committee Membership:

J. W. McClory, PhD
Chair

Col. J. R. Fee, PhD
Member

B. F. Akers, PhD
Member

S. R. McHale, PhD
Member

AFIT-ENP-DS-20-S-027

Abstract

This dissertation describes the verification and validation of methods for producing radiation protection factors (RPFs) using experiments and Monte Carlo N-Particle 6 (MCNP6) simulations. RPF validation of a steel enclosure using a plutonium-beryllium source produced a validated RPF of 1.187 ± 0.003, with statistically significant agreement between neutron MCNP6 models and experiments and a gamma protection factor (GPF) with statistically significant agreement to the measured GPF with a 95% confidence interval. Efforts to validate more complex enclosures using the Fast Burst Reactor (FBR) yielded the first-ever direct measurements of this reactor's prompt gamma emission spectrum and revealed irreconcilable differences between the FBR facility-provided source spectrum and spectrometer measurements, resulting in modeled GPFs 27% to 106% higher than experimental GPFs. The use of a tallying annulus reduced the variance in simulations of the FBR's projected radiation field by three orders of magnitude. Annulus-based tallying enabled the demonstration of a nuclear weapon-like irradiation of a target at 1400 meters, yielding statistically significant gamma and neutron flux spectra in 36 hours using a laptop computer with an i7-4700MQ processor. The effects of different simulation and calculation methods on RPFs are examined and discussed, along with recommendations and lessons learned for future work.

Acknowledgments

I thank God for blessing me with the many people and organizations who have supported, encouraged, and sustained me throughout my studies at AFIT.

I would like to express my sincere appreciation to my faculty advisor, Dr. John McClory, for his guidance and support throughout the course of this effort. His insight and experience were invaluable to this work. I would also like to thank my committee members for their support throughout this process.

I am deeply grateful to my wife and children for their love and encouragement throughout my PhD studies and candidacy.

I am deeply grateful to the United States Army, the Ohio Army National Guard, and the Army Reserves for the opportunity to serve as a soldier throughout my PhD studies, and I am deeply grateful to the United States Air Force and the School of Aerospace Medicine for the opportunity to apply my passion for nuclear engineering and radiation research to my ongoing career.

I dedicate this dissertation to the memory of my grandfather, best man, and surrogate father, William W. Erwin, whose memory continues to inspire my best efforts in service of family, country, and God.

William J. Erwin

Table of Contents

Page

List of Figures

Page

List of Tables

Page

VERIFICATION AND VALIDATION OF RADIATION PROTECTION FACTORS FROM MONTE CARLO SIMULATIONS

I. Introduction

Shortly after the discovery of radioactivity in 1896, evidence of negative health effects from ionizing radiation surfaced as X-rays became widely used [1, 2, 3, 4, 5]. In subsequent years, humanity became increasingly aware of the dangers associated with ionizing radiation. A vast body of research has consistently demonstrated that doses above 200 mSv of penetrating ionizing radiation present measurable health risks to personnel, and protection standards have become more specific and more restrictive with time by various authorities on the matter since these risks became apparent [6, 7, 8, 9, 10]. Two modern standards dominate radiation dosimetry: those of the International Commission on Radiological Protection and those of the United States Nuclear Regulatory Commission.

For nearly a half century after the discovery of radioactivity, the threat of ionizing radiation was limited to people working in the field of X-ray research, people working with medical equipment, and people working in a few industrial applications. Although the military used radioactive radium in dials and watches as early as World War I [11], weaponized radiation only became a practical option with the success of the Manhattan Project in 1945. For the first time, a deliverable weapon could kill many thousands using ionizing radiation.

1.1 Weaponized Radiation and Military Vulnerability Studies

The short-term, acute effects of radiation are widely known and documented. Figure 1 illustrates these risks, as well as excess cancer risk observed in atomic bomb survivors. An dose of 1 Gray or 100 rads can cause acute radiation sickness, including vomiting, weakness, and an increased susceptibility to infection for 24 hours, with some residual effects lasting as long as a month, but is not generally fatal by itself [12]. The number of symptoms, their severity, and the likelihood of death increase with higher doses, with a 10 Gray dose killing nearly 100% of patients, even with modern medical treatment.

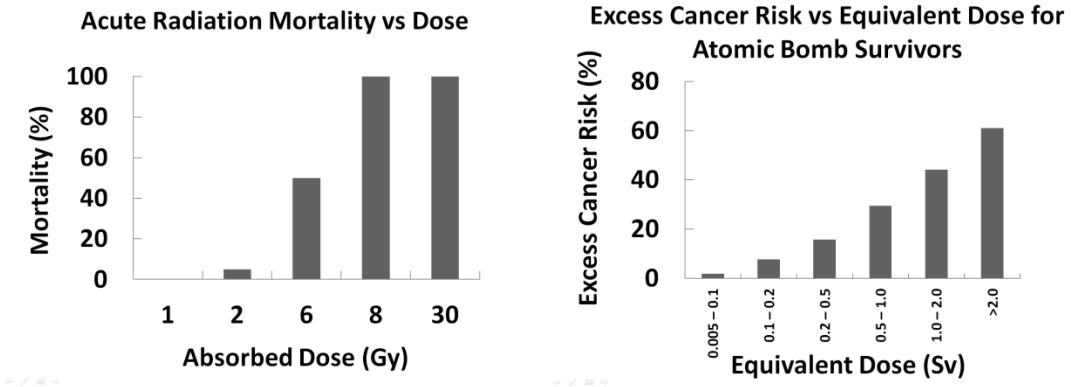

Figure 1. Mortality vs Dose for acute radiation syndrome with treatment, recreated from Merck (left) [13], and Excess Cancer Risk vs Equivalent Dose for Atomic Bomb Survivors, recreated from Preston (right) [14].

Even spread out over time, radiation doses can lower life expectancy and reduce quality of life by increasing cancer risks, and no threshold dose or dose rate at which these risks begin has been established [15]. Although recent research has shown that populations in areas of high background radiation tend to live 2.5 years longer than populations in areas of low background radiation [16], the risk posed by low-dose radiation is a subject of contentious debate among health physicists. Social and psychological factors driven by

radiophobia can compound risk from actual exposures; simply working near a major nuclear event is associated with stigmas, anxiety, depression, suicide, and post-traumatic stress [17]. These effects gave rise to serious concerns in the United States military after the successful Soviet nuclear weapon test of 1949.

During the nuclear arms race of the Cold War, the United States investigated the threats of penetrating ionizing radiation through robust experimentation and several modeling methods. These efforts included nuclear weapon tests, dedicated radiation test facilities, and three methods of mathematical modeling [18, 19, 20]. Chapter 2 describes these efforts in more detail. In the decade following the fall of the Soviet Union, the majority of these dedicated test facilities closed. However, several international developments since the end of the Cold War have led to a renewed interest in assessing the situational threats of ionizing radiation. These developments include proliferation and nuclear weapons tests by Pakistan and India, nuclear weapons tests by North Korea, and an ambitious Iranian nuclear program. These resurgent nuclear threats, however, have not led to renewed funding for nuclear vulnerability test facilities [21]. Without the irradiation facilities available to previous generations, understanding of the degree of protection provided by the U.S. military's fleet of vehicles has atrophied as the Department of Defense has replaced older vehicle designs and models.

Post Cold War: Rising Tensions, Renewed Interest, Fewer Resources

This lack of understanding became uncomfortably clear during the United States' emergency relief efforts to Japan following the massive earthquake and tsunami in the spring of 2011. When operational leaders requested radiation protection information for

their vehicles and shelters, none was available because the Department of Defense no longer required the Army to acquire or catalogue that information. Radiation protection data had been eliminated as a cost-cutting measure [21, 22]. As a result, operational leaders had to make radiation risk management decisions with inadequate knowledge of vulnerabilities. This incident demonstrated that radiation threats to military personnel are not unique to the nuclear battlefield.

In response, the Defense Threat Reduction Agency (DTRA) and US Army Nuclear and Countering Weapons of Mass Destruction Agency (USANCA) are funding a long-term plan to assess the radiation protection provided by modern Army vehicles to their crews and passengers. However, neither agency has the resources to recreate the radiation testing infrastructure of the Cold War. Accordingly, the focus of this assessment plan has shifted away from pure experimentation.

Although current radiation test facilities cannot support robust radiation protection experiments, developing technology may allow for radiation protection evaluations by computer modeling. Modern computers allow for approximately nine orders of magnitude more calculations per second than computers of the Cold War [23]. Figure 2 shows unabated, exponential growth in the world's fastest computers since the early 1960s. If radiation models can reproduce experimental reality to an acceptable tolerance, then those simulations could provide a cheaper, faster, and more flexible alternative to radiation testing facilities. Since 2011, The Defense Threat Reduction Agency has been investigating the utility of Monte Carlo N-Particle version 6.1 (MCNP6.1) to produce radiation protection factors in lieu of extensive and expensive radiation testing programs [22].

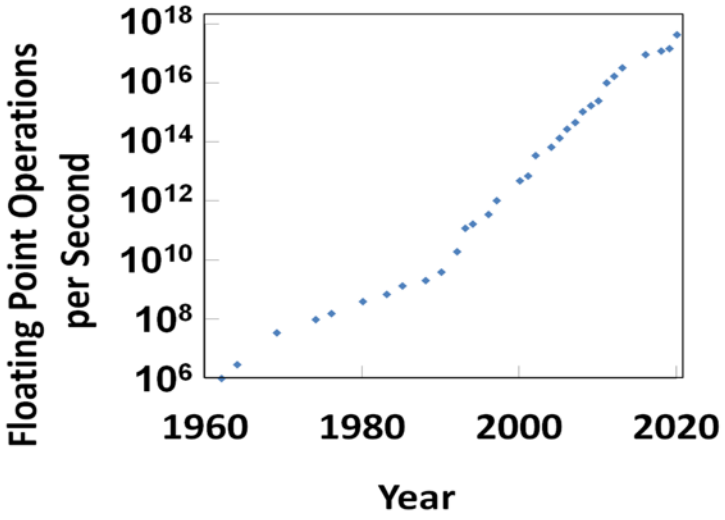

Figure 2. Processing speed of the world's fastest computers by year. Recreated from Top 500 data [23].

Developments since the inception of this radiation protection assessment plan underscore its importance. In addition to further nuclear weapons tests by North Korea, tensions with Russia have been marked by breakdowns in nuclear cooperative agreements and heightened international tensions. Russia's nuclear posturing has included exercising strategic weapons platforms near the borders of the United States [24, 25], ending several cooperative agreements on reducing both nations' stockpiles of highly-enriched uranium and weapons-grade nuclear fuels [26, 27], and breaking the Intermediate-Range Nuclear Forces (INF) Treaty by deploying a battalion of medium-range ground-launched cruise missiles [28]. Chinese nuclear modernization, Iran's nuclear ambitions, and the threat of nuclear terrorism have also contributed to an increased national focus on nuclear threats. President Trump publicly stated his intention to strengthen and expand nuclear capability and voiced concerns about an unstable global mindset on the subject of nuclear weapons

[29], and the 2018 Nuclear Policy Review lists "Achievement of U.S. objectives if deterrence fails" as a critical role in U.S. national security strategy [30]. Strengthening and expanding the United States' nuclear capability and achieving U.S. objectives if deterrence fails depends on understanding the military's nuclear vulnerabilities and protection measures.

1.2 Problem Statement

The purpose of this research is to develop and validate a method for determining the radiation protection factor provided by a shielding vehicle to personnel within against externally applied gamma and neutron radiation fields using MCNP6.

MCNP6 is a general-purpose Monte Carlo N-Particle code that models radiation transport in three-dimensional geometries. Written in FORTRAN, the program is the latest in a continual development effort by Los Alamos National Laboratory dating back to the 1950s [31].

A Radiation Protection Factor (RPF) is a unit-less number describing the relative benefit provided by a shielding structure in reducing the acute health effects of ionizing radiation. Higher RPFs are associated with greater protection and lower doses so that, from the perspective of a shielded person, bigger is better.

For the purposes of this research, the types of ionizing radiation investigated are limited to gamma radiation and neutron radiation. Although alpha and beta radiation can produce health effects, they can be effectively shielded with skin and clothing at energies associated with nuclear explosions and radioactive materials. Alpha and beta radiation is most threatening in the form of contaminating radioactive residue and fallout that is inhaled

or ingested. Rudimentary protective measures such as clothing, gloves, good hygiene, and a high-filtration respirator can effectively manage these risks. However, such protection measures are useless against gamma and neutron radiation, which requires larger and more massive shielding than is practical for worn equipment. A vehicle, however, can offer some protection from neutron and gamma radiation. This protection is important for radiation health effects, which come in two general categories: short-term deterministic effects and long-term stochastic risks. Table 1 provides a useful reference for the properties, terms, and primary health threats associated with each category of radiation health effects.

Table 1. Categories and terms of radiation health effects and their associated properties, units, and health threats, recreated with information from Cember [15].

	Deterministic Health Effects	**Stochastic** Health Effects
Driving Property	**Dose**	**Dose Equivalent or Equivalent Dose**
Method of Calculation	**Energy Deposited / Mass**	**Dose * weighting factors**
U.S. Units	**rad**	**rem (roentgen equivalent in man)**
International Units	**gray (gy)**	**sievert (sv)**
Primary Health Threat	**Acute Radiation Syndrome starting ~1 gy**	**~1% Increased risk of fatal cancer per sv, undetermined threshold**

When considering radiation health effects, most regulations and guidance focus on long-term cancer risks and reducing doses in accordance with the well-known concept of "as low as reasonably achievable" or ALARA. These stochastic risks are quantified by the dose quantities of equivalent dose and dose equivalent, both in units of sieverts and rem,

and they account for the tendency of doses from radiation types with high linear energy transfers, such as neutrons, to cause higher risks of cancer than radiation types with more diffuse energy deposition such as gamma rays. Equivalent doses under 0.5 sieverts have no symptoms that are likely to impede personnel effectiveness in a physical sense. However, concerns about health risks from exposure to radiation disasters and nuclear attack stemming from persistent myths and misperceptions about the threat of radiation have been shown to cause significant psychological issues including depression, anxiety, and paralyzing fatalism [32, 33]. Reliable information on a vehicle crew's protection from radiation effects may help to address and assuage these concerns and increase crew effectiveness in elevated radiation fields.

While the long-term stochastic health risks of ionizing radiation doses are an important field of research in their own right, it is the short-term threat of acute radiation syndrome that is of foremost concern to both military operations and nuclear disaster response. Whether in a tactical situation or an emergent lifesaving disaster response, the primary concern of military forces is the accomplishment of the mission, and it is the acute dose as measured in gray that poses a physical threat to the ability of personnel to execute the mission. Thus, both dose in grays and equivalent dose in sieverts are important for this work, and differences between radiation protection factors computed by each method merit investigation and comparison.

1.3 Research Goals and Objectives

This project has three goals and eight total supporting objectives.

1. Create a RPF evaluation method that uses experimentally-validated MCNP6 simulations.
    a. Establish MCNP6 neutron transport validation techniques.
    b. Establish MCNP6 gamma transport validation techniques.
    c. Establish a procedure for normalizing the gamma and neutron dose components in a simulated scenario.
    d. Establish a procedure for computing the resulting doses and total RPF.
2. Demonstrate this method on a series of surrogates using a plutonium-beryllium (PuBe) source and a nuclear reactor.
    a. Measure and validate the gamma emission spectrum of the fast burst reactor (FBR).
    b. Demonstrate the RPF method on a simple steel surrogate.
    c. Demonstrate the RPF method on a three-material surrogate.
    d. Demonstrate the RPF method on a complex geometry surrogate.
3. Build a computer model of a Stryker vehicle irradiated by a nuclear weapon spectrum in Software for Optimization of Radiation Detectors (SWORD) and run it in MCNP6.

Several terms used in these goals and supporting objectives will be explained in more detail in later chapters. The RPF evaluation method consists of a series of simulations and computations that can be validated with neutron and gamma irradiation experiments. The principles behind this method will be described in Chapter 2, and the overall algorithm will be described in detail in Chapter 3. Although MCNP6 is distributed with VisEd, a

geometry visualization program, it can be difficult to ascertain from VisEd whether complicated geometries in simulations are adequately described in an MCNP6 input deck. One solution to this is using SWORD, a program allowing 3-dimensional visualization and construction of a virtual radiation environment and subsequent input deck building for MCNP6 simulations. The PuBe source is a radioactive source that emits neutrons and gamma rays. The surrogates described are box-like constructions of varying sizes, wall thicknesses, and materials which allow nuclear instrumentation to detect gamma and neutron fluxes within their enclosures.

In addition to its overall purpose, this dissertation includes several contributions to the field of nuclear engineering. The first is an experimentally-validated MCNP6 RPF assessment of a steel enclosure that combines gamma and neutron radiation simulations and measurements. The second is the first-ever direct measurement of the FBR's gamma output spectrum and an evaluation of its gamma emission spectrum. The third is a method of conducting RPF assessments of nuclear strikes against newer types and models of tactical vehicles which the U.S. Army has not experimentally assessed for radiation protection due to their development and fielding after the Cold War.

One of these goals has already been accomplished in preliminary work. MCNP6 neutron protection factors (NPFs) were validated on a simple steel enclosure using a PuBe source, a deuterium-deuterium (D-D) neutron generator, and the Fast Burst Reactor (FBR) at White Sands Missile Range [34]. Gamma protection factors (GPFs) were validated on a simple steel enclosure using radioisotopes and the FBR [35]. Much of this research, as well as parallel efforts across DoD, have already been published [22, 36, 37, 38].

1.4 Investigative Questions

Pursuant to the goals and objectives, several key questions were investigated:

1. What are the steps involved in producing a RPF for a given scenario using MCNP6?
2. How reliably can MCNP6 transport gamma and neutron radiation in various shielding scenarios, and how should this reliability be enumerated?
3. What additional considerations and techniques are necessary to produce a reasonably reliable RPF for a given scenario within practical limits of computational power and time?

II. Background and Theory

2.1 Radiation Protection Research during the Cold War

A reasonable starting point for considering the protection offered by military vehicles to personnel is historical examples. However, the effects of the bombings on Hiroshima and Nagasaki, though well documented, offer little insight into the relative vulnerability of military formations to nuclear weapons. Although we can infer some effects information regarding the vulnerability of personnel with no obstructing shielding between themselves and the fireball, the majority of shielded personnel were inside buildings, not armored military vehicles. Furthermore, in the case of the Hiroshima bombing, the light wood and paper construction of most of the buildings in the city led to firestorm conditions which killed a great number of people. Coupled with the blast, thermal, and secondary effects of the explosions, these made for a combination of confounding variables that would take decades of determined study to characterize and isolate from the specific health effects of nuclear weapon radiation [39]. As a result, in the late 1940s, the U.S. military faced a substantial lack of information on their vulnerabilities to the unique radiation effects of the atomic bomb.

Following the war, the Navy sought to investigate the effects of nuclear weapons on naval vessels in a three-shot series named Operation Crossroads. The intent of Crossroads was to demonstrate the fleet's survivability and resilience against nuclear weapons. The blast and thermal effects of the air-dropped weapon test, Able, sank five ships and caused damage and fires on an additional fourteen. The prompt radiation from this explosion killed about 50% more of the test animals than other effects. Of particular

note was the case of the battleship Nevada, which survived the blast without sinking, but suffered 100% test animal casualties from the prompt radiation. The second test, Baker, was detonated 30 meters underwater, and the relative effects of radiation were even more pronounced. The blast and hydrodynamic effects sank nine ships, but more importantly, every target ship became almost irreversibly contaminated, and nearly every test animal died of acute radiation effects. Attempts to decontaminate most of the target ships were aborted after dozens of personnel took unacceptably high doses, and the third Crossroads test was cancelled. Most of the target ships had to be scuttled rather than scrapped, and many of the support vessels required extensive decontamination before returning to service [40]. Both Crossroads tests demonstrated the vulnerability of a vehicle's crew, and how an otherwise fully mission-capable vehicle may be unusable or unsafe for extended periods after withstanding a nuclear bombardment.

Understanding the vulnerability of military formations to nuclear weapons became especially important in 1949, when the Soviet Union detonated its first nuclear weapon. The U.S. Army conducted its first military effects testing during the Buster-Jangle series of nuclear weapons tests at the Nevada Test Site in 1951. Military exercises in conjunction with nuclear tests became a regular feature at the Nevada Test Site for the rest of the 1950s, with formations of soldiers maneuvering around and observing test explosions during operations Tumbler-Snapper, Upshot Knothole, Teapot, and Plumbob. Many of these tests included examining radiation effects on surrogate animals. The last U.S. nuclear weapons tests during Operation Sunbeam evaluated several tactical nuclear weapons. From this point on, the Partial Test Ban Treaty was in effect, and further radiation vulnerability research required a different approach [41].

One test from this era was particularly notable for demonstrating the capability of armored vehicles to operate in a nuclear battlefield: the Apple 2 test at the Nevada Test Site during Operation Teapot in 1955. Immediately after a 29 kT detonation atop a 500-foot tower, approximately 1,000 soldiers in an armored formation called Task Force Razor drove to within 820 meters of the blast site as a mushroom cloud formed overhead. Upon reaching a threshold of 1 rad per hour inside the lead tanks, the task force turned and maneuvered around ground zero to assault a nearby objective. Radiation monitors tracked exposures, both outside and inside the vehicles, as well as to all participating personnel [42].

While the Apple 2 test conclusively proved that the 1955 fleet of vehicles and crews could operate in the vicinity of a nuclear attack, it was never repeated. Although it is possible to extract some information about the radiation protection provided by the vehicles from the test data, Task Force Razor was intended to demonstrate capabilities and build confidence for tactical formations, not to specifically evaluate the M48 tanks and M59 armored personnel carriers used.

Following the implementation of the Partial Test Ban Treaty, military vehicle susceptibility to ionizing radiation had to be evaluated by analogous radiation sources. Several test facilities were constructed during this time. For example, the AURORA X-ray facility evaluated vehicle shielding in high-energy photon radiation fields. The United States produced and operated several fast burst reactors made of bare, weapons-grade uranium, that produced gamma and neutron spectra that were very similar to those of a fission-only nuclear weapon. These reactors included Lady Godiva, Godiva II, the Army Pulse Radiation Facility, and the Fast Burst Reactor. This allowed limited testing of

components and vehicles to weapon-like radiation spectra and fluences [43]. The Army Pulse Radiation Facility was specifically dedicated to radiation testing of vehicles and vehicle components [44, 45].

2.2 Radiation Research: Fall of the Soviet Union to Present

Following the end of the Cold War, funding priorities shifted away from defense spending in general and nuclear weapons effects research in particular. The United States went into an indefinite weapons testing moratorium in October of 1992, cutting short planned underground nuclear testing. The Army stopped evaluating the protection offered by its combat vehicles and discontinued publishing AR 70-60: Army Nuclear Survivability. It was replaced with AR 70-75: Survivability of Army Personnel and Material in 2005 [46], which delegates the writing of standards for chemical, biological, and nuclear threats and establishes procedures for ignoring those standards.

Current hold-over facilities from the Cold War tend to be less specialized in their applications, and many overlapping capabilities have been eliminated. The only remaining reactor in the United States capable of creating a spectrum of radiation from a bare, un-moderated reactor in a prompt, supercritical mode is the Fast Burst Reactor at White Sands Missile Range, New Mexico. This reactor is of particular interest, as it can be operated outdoors, providing measurable radiation environments similar, though far smaller in magnitude, to those of a fission weapon [47].

2.3 Non-Military Research

The subject of vehicular radiation shielding has been extended into other applications. As NASA works toward the goal of manned interstellar missions, the threat of radiation to astronauts in deep space is a major concern. Solar events can create both heavy charged particle radiation and neutron radiation within a spacecraft through proton-neutron nuclear reactions [48]. Additionally, cosmic radiation consisting of heavy charged particles and gamma rays can contribute significantly to an astronaut's dose during a deep space mission [49]. The mass-limited nature of spacecraft design poses a challenge for understanding and optimizing protection for direction-dependent incident radiation fluxes [50]. Data presented in Figure 3 shows how astronauts on interplanetary missions can expect to receive far greater cumulative doses than even the elevated doses they currently receive on ISS missions.

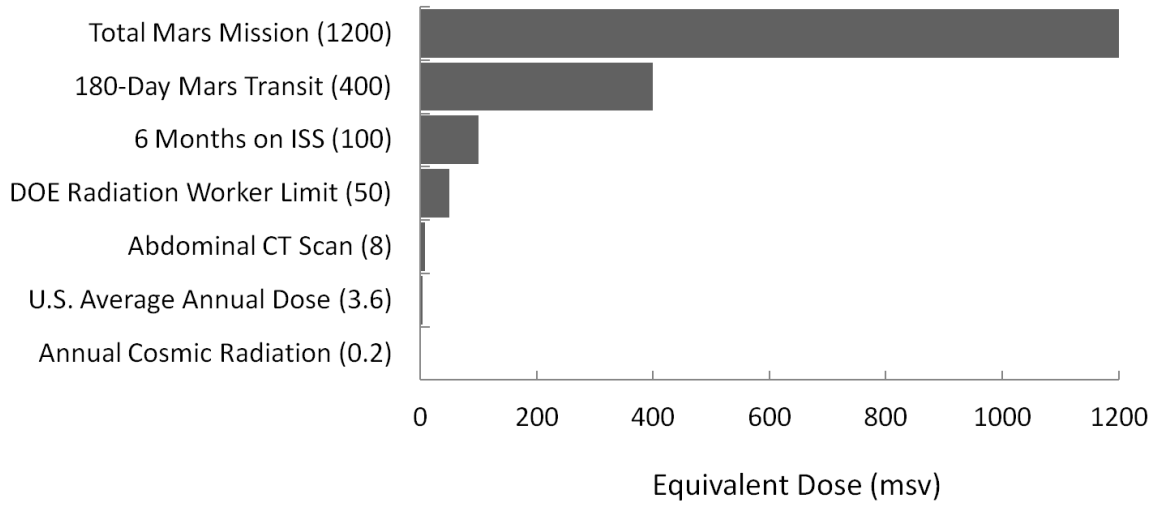

Figure 3. Comparison of benchmark doses with doses of interest to manned space missions. Recreated from NASA [51].

Civilian research into shielding has also been motivated by the need to protect personnel and property during responses to radiological and nuclear accidents. Such research tends to peak after significant accidents [52]. The Fukushima disaster has sparked renewed interest in responding to nuclear emergencies and highly radioactive areas. Recent difficulties in recovering damaged fuel that escaped the Fukushima reactor core highlights the need for effective mobile shielding, even for robotic platforms, due to the vulnerability of their electronics to doses over 100 Grays [53].

2.4 Radiation Shielding Theory

Gamma ray interactions with matter primarily consist of photoelectric absorption, Compton scattering, and pair production [54]. For energies typically associated with nuclear weapons between 100 keV and 4 MeV, Compton scattering is the dominant interaction for most materials [55]. Since Compton interactions and photoelectric absorptions take place between gamma rays and electrons, effective gamma ray shielding tends to be made of heavier elements with a high density of electrons.

Neutrons interact with atomic nuclei primarily by scattering collisions and absorption. Fast neutrons are not generally absorbed in most shielding materials until they have thermalized (slowed down) through a series of collisions with nuclei. In contrast to the materials used in gamma shielding, effective neutron shielding has two key components. The dominant component is hydrogen atoms, which provides the ability for protons to maximize collision energy transfer, and the other is a material which can readily absorb thermalized neutrons. Absorption can be increased significantly by adding a material with a particularly large neutron capture cross section to a thermalizing material.

Three well-known thermal neutron absorbers are specific isotopes of boron, gadolinium, or cadmium [56], all of which are commonly used in conventional nuclear power reactors' control rods and emergency shutdown systems to reduce the neutron population and slow or stop the fission chain reaction.

Computing Dose: Flux-to-Dose Conversion

As discussed in the previous section, high-energy photons associated with nuclear weapon radiation tend to impart their energy to electrons [57]. These energy depositions tend to be distributed over an energy and material-dependent range of depths. The subsequently excited electrons tend to scatter and distribute energy through a wider volume of material than a heavy charged particle [15]. Thus an interacting gamma ray flux tends to create a low density of ionizations in a target material.

Elastic scattering neutrons tend to deposit considerable energy to a target nucleus, which becomes a heavy charged particle [54]. Such interactions tend to cause a high density of ionizations in a relatively small volume. In living tissue, this density of ionizations leads to concentrated damage to DNA and proteins that is more difficult to properly repair than the lower-density damage created by gamma rays. Therefore, high energy neutron fluxes tend to increase long-term stochastic health risks more than their doses would ordinarily indicate, an effect accounted for by applying energy-dependent weighting factors to neutron flux spectra. The NRC and ICRP have slightly different standards of weighting factors for computing the dose equivalent or equivalent dose for energy groups of neutrons [15].

From Cember's Health Physics, a flux of photons in a given material can be converted into an exposure and a dose rate, and this flux-to-exposure-to-dose rate conversion is valid for photon energies up to 4 MeV [15]. The dose rate is given in Grays per second as

$$\dot{D}_{gE} = \frac{\phi\left(\frac{photons}{cm^2 \cdot s}\right) \cdot E\left(\frac{MeV}{photon}\right) \cdot \left(1.6 \cdot 10^{-13} \cdot \frac{J}{MeV}\right) \cdot \mu_m \cdot \left(\frac{1}{cm}\right)}{\rho_m \cdot \left(\frac{kg}{cm^3}\right) \cdot \frac{J/kg}{Gy}}, \quad (1)$$

where ϕ is the flux of monoenergetic photons per square centimeter per second, E is the energy of each photon, $\mu_m$is the linear energy absorption coefficient for the target medium, and $\rho_m$is the density of the target medium. By summing this expression over m energy bins in a given spectrum, the total dose rate can thus be computed as

$$\dot{D}_g = \sum_{i=1}^{m} \frac{\phi_i\left(\frac{photons}{cm^2 \cdot s}\right) \cdot E_i\left(\frac{MeV}{photon}\right) \cdot \left(1.6 \cdot 10^{-13} \cdot \frac{J}{MeV}\right) \cdot \mu_{mi} \cdot \left(\frac{1}{cm}\right)}{\rho_m \cdot \left(\frac{kg}{cm^3}\right) \cdot \frac{J/kg}{Gy}}. \quad (2)$$

By log-log interpolation of tabled linear energy absorption coefficients for soft tissue, a cumulative dose can thus be calculated from a known gamma ray flux

A variety of neutron flux-to-dose equivalent tables have been published [58, 59, 60, 61, 62, 63]. The conversion coefficients in these tables are normalized to the unit of radiation fluence and provided in units of Sv-cm^2 or rem-cm^2. The product of these conversion coefficients and the incident radiation fluence then gives the dose equivalent, in Sv or rem. The result is meant to indicate the increased risk of long-term stochastic health risks, not short term deterministic effects. Such tables require mathematical manipulation to remove weighting factors for neutron energies. By dividing the dose

equivalents in sieverts by the energy-dependent weighting factors, such tables can be modified to provide the dose in gray. Using a log-log interpolation of the adjusted dose equivalent chart to find the dose for *m* energy bins, we can calculate a neutron dose rate as

$$\dot{D}_n = \sum_{i=1}^{m} \phi_i \left(\frac{neutrons}{cm^2 \cdot s}\right) \cdot \frac{D_{ni}}{\phi_i} \left(\frac{Gy}{\frac{neutrons}{cm^2}}\right), \tag{3}$$

where ϕ_i is the neutron flux for the *ith* energy bin and D_{ni} is the dose rate associated with one neutron per second of the *ith* energy bin.

Gamma and neutron energy spectra for various unclassified nuclear weapon sources are tabulated by DTRA [64]. While these spectra can no longer be directly measured due to the moratorium on nuclear weapons testing that has been in place since 1991, they provide useful benchmarks which can be compared to the experimentally verifiable simulations of this work. This is the basis with which it is possible to model gamma ray and neutron shielding provided by a vehicle.

Importance of 3-Dimensional Geometry and Scattering

Scintillation detectors have been widely used to detect ionizing radiation. In most applications, their principles of operation are similar. Ionizing radiation deposits its energy within the scintillating crystal, exciting electrons in the atoms of the crystal lattice. These atoms' electrons de-excite or "fluoresce," releasing a number of photons proportional to the energy deposited. The crystal itself is transparent to its own fluorescent photons, allowing them to be collected on a photocathode which releases a number of electrons ideally proportional to the number of fluoresced photons. By accelerating the electrons

released by the photocathode in a series of electric fields into metal plates, these electrons are multiplied and collected at an anode, producing a signal that can be subsequently amplified and processed into discrete pulses. This photon-to-signal process is contained in a device known as a photomultiplier tube. In the case of gamma radiation, the height of the produced pulse corresponds to the energy of the interaction within the detector, which is driven by the energy of the incident gamma ray and the materials of the scintillator [54].

In the case of a scintillator used to detect thermal neutrons, a neutron is captured within the scintillator and causes a nuclear reaction. In most cases, the heavy charged particles resulting from that nuclear reaction are captured within the scintillator, depositing their kinetic energy within the fluorescent material. From that point, the process is the same as in a gamma scintillator, but the nature of the neutron capture means that the spectrum produced consists of discrete peaks defined by the nuclear interactions and the properties of the detector material itself, not the energy of the neutron.

Thus thermal neutron detectors do not give spectral information about the neutron flux, because they only detect thermal neutrons. Rather, they provide a count rate of particular neutron interactions within the detector. One method of attaining a neutron energy spectrum using such a detector is to take multiple observations of neutron count rates of a LiI scintillator placed within polyethylene spheres, known as “Bonner spheres,” of varying radii. The hydrogenous polyethylene spheres act to moderate (decrease neutron speeds of) the neutron flux to varying degrees, and the scintillator then detects those neutrons that are thermalized. By building a library of expected response functions for the detector within each sphere, it is possible to mathematically unfold a neutron spectrum.

Another method of neutron spectroscopy commonly used in high-flux experiments is foil activation spectroscopy. In this approach, an array of materials is exposed to a neutron flux. After the irradiation, each material is separately evaluated to determine the amount of neutron-activation. Using known energy cross section data to define the appropriate expected response of each material, it is then possible to unfold a neutron energy spectrum. This technique has the advantage of only requiring a single irradiation to produce a spectrum. However, it requires higher fluxes than the Bonner sphere spectroscopy method to obtain statistically significant results [65].

Vehicle/Equipment vs. Personnel Vulnerability

While this research focuses on radiation threats to personnel, some systems on modern armored vehicles are susceptible to degradation and loss of function when subjected to high fluences of radiation. While vehicles in the 1950s were subjected to radiation from atmospheric nuclear weapons tests, as previously described, there were no operational effects at the dose levels they received. This does not necessarily mean that modern vehicles would be as intrinsically resilient. Electronic systems, which play more important roles in modern vehicles than their 1950s counterparts, are particularly susceptible, and modern electronics are more susceptible than those of previous generations. However, the doses to electronics that are required to produce any detectable effect in modern or antiquated electronics are one to two orders of magnitude greater than doses associated with a 100% chance of death from short-term, deterministic radiation health effects [53, 66]. Therefore, vehicle crews are the weak point for any vehicle unless that vehicle can reduce radiation doses to occupants by a factor of a hundred or more.

Equipment vulnerability is a related concern that has received relatively little attention. Even before the end of the Cold War, the United States Army fielded most of its equipment without considering its survivability in a nuclear weapon environment. Nuclear survivability was only included in the equipment procurement process beginning in 1977, with the philosophy that a soldier's essential equipment should survive nuclear attack at least as well as the soldier. This approach is justified; with the notable exception of EMP, most prompt nuclear weapons effects that would degrade or destroy a soldier's equipment would easily kill the soldier [67].

2.5 Modeling Radiation Shielding

A rough first-order approximation of one-dimensional radiation shielding for photons can be calculated using a simple attenuation formula,

$$\boldsymbol{\varphi_{out} = \varphi_{in} e^{-\mu \rho t}}, \tag{4}$$

where φ_{out} is the flux leaving a barrier, φ_{in} is the flux entering the barrier, μ is the mass attenuation coefficient specific to the energy of the photon flux, ρ is the density of the barrier material, and t is the thickness of the barrier. Attenuation coefficients for both photon fluxes and photon energy fluxes are available from NIST [68]. Although it is possible to select a single representative energy and compute an approximate reduction in flux energy using that energy group's attenuation coefficient, such a technique must be calibrated to a chosen shielding scenario. Such a calibration will lose accuracy as the energy spectrum changes with distance from a radiation source due to interactions in air and ground and secondary radiation from neutrons. This simple model will also lose

accuracy for barriers that cannot be approximated as simple slabs because of angular scattering. Finally, this simple one-dimensional model only accounts for simple one-dimensional fluxes, not for an angular distribution of incoming radiation. The advantages of this approach are its computational efficiency and simplicity, as the simple attenuation model can provide a good approximation of many shielding scenarios in a single mathematical operation.

Semi-Empirical Formulas

An improved method for determining reductions in incoming radiation due to a shielding structure is described in Charles Eisenhauer's "An Engineering Method for Calculating Protection Afforded by Structures Against Fallout Radiation [69]," which accounted for some photon scattering in slab geometries via buildup factors. This approach replaces the exponential attenuation model with charts and tables derived from simulations and nuclear testing. Additionally, the geometry of angular intensity distributions for incoming radiation allows for a better approximation of incoming shielding. However, once the thickness of a shield from an angular flux component is calculated, the engineering method continues to treat all shielding structures as one-dimensional barriers. Thus, the engineering method does not account for angular scattering within a structure, second-order radiation brought on by neutron interactions, or different energy spectra. The reduction factors produced are only somewhat improved from first-order approximations [69].

Discrete ordinates offer an alternate shield-modeling approach. By discretizing a shielding volume into a series of zones and approximating the probabilities of different

types of interactions and their outcomes into discrete angular and energy flux groups, this method is capable of modeling some of the geometric and physics interactions with relatively good computational efficiency. There are two key drawbacks to using discrete ordinates. First, they are not intrinsically accurate, but must be set up and adjusted to become so. Discretations of space and energy must be selected that approximate a reality of distributed locations and energies within a radiation shielding scenario. Without some experimental verification on the fluxes of a discrete ordinates simulation, it is difficult to ascertain the accuracy of this method; output data from discrete ordinates simulations tend to be deceptively smooth, suggesting a much smaller margin of error than should exist. The second drawback of discrete ordinates simulations is a lack of portability. A discrete ordinates simulation in one scenario may require significant adjustments to its chosen energy, angle, and location groups for different geometries, materials, types of radiation, and input energies. A variety of discrete ordinates techniques and approaches have been applied to radiation shielding simulations for the last half century [70, 71, 72, 73].

Monte Carlo radiation transport applications considering human dosimetry have been the subject of development since the 1950s [74]. These methods provide the most reliable and accurate simulation technique for measuring radiation transport in shielding applications. By randomly sampling a particle's direction, distance to interaction, type of interaction, and the outcome of each interaction (among other parameters), one particle at a time, and iterating this process many times in a computer, a Monte Carlo approach closely matches the probabilistic features of radiation transport as observed in nature.

Tallying is the method by which Monte Carlo simulations produce useful information. A tally in a Monte Carlo simulation establishes conditions under which a

tracked particle will be counted, as well as the method by which it is counted. For example, a tally could count all particles crossing into a simulated detector surface and sort that tally into energy bins, creating an energy flux spectrum. Alternately, a tally could count the number of interactions within a simulated detector and sort these interactions by their energies, creating an energy deposition spectrum. Whatever the definition of the tally, the useful information comes from the statistical data collected. By counting large numbers of particles crossing into or interacting within regions of interest inside a three-dimensional model, it is possible to collect statistical data on radiation transport that closely models reality.

The accuracy of these models depend on the fidelity of the three-dimensional model to its real-world counterpart, the fidelity of the radiation source spectrum to its real-world counterpart, the accuracy of the simulation's interaction cross section library, and the accuracy of the simulation's interaction sampling algorithms. The precision of such models depends on two factors. The first factor is the computational efficiency of the simulation, which is a comparison of the number of particles tallied versus the number of original particles generated. The second factor is the raw number of original particles created [31].

Since the computational efficiency of most Monte Carlo shielding simulations tends to be intrinsically low, the Monte Carlo approach generally requires many sampling operations in order to yield statistically useful data. This was a significant problem during the Cold War, when computers were orders of magnitude less powerful than today, limiting simulations to small sizes. Modern computers are capable of yielding statistically significant data for less computationally efficient simulations in far less time [35]. Further

improvements in computational efficiency have been developed using techniques collectively known as variance reduction methods.

One method for improving the computational efficiency of Monte Carlo methods is to use it in conjunction with discrete ordinates methods. An example of this is the Vehicle Code System (VCS) program developed at Oak Ridge National Laboratory in the early 1970s and updated until 2001. It is still available from the National Nuclear Security Administration, though its updates were apparently developed for compatibility purposes only, as the user's manual has not been updated since 1974 [75, 76]. VCS was intended to solve the same problem as this research. VCS coupled radiation transport in air using discrete ordinates methods with a Monte Carlo approach in the shielding itself. Its developer claimed it could calculate the dose from a low-yield nuclear explosion within 1 km of a tactical vehicle at a variety of angles. According to documentation, the program took two and a half hours to run from beginning to end, with additional 25-minute evaluations of different angles, if desired, on an IBM 195 computer, which was the most powerful IBM model as of 1970. Given that modern computers are orders of magnitude more powerful; this code could likely run on a modern computer in a few minutes or less. The vehicle models were simple geometric shapes and the cross section library and discretized input spectra were imprecise by modern standards, but the Monte Carlo code for transporting the radiation was a true three-dimensional simulation which produced partially validated spectra for neutron and gamma radiation. Though crude by modern standards, the fundamental process of VCS allowed for gamma and neutron spectra, doses, and radiation protection factors to be simulated within a vehicle. Unfortunately, the full

process was never experimentally validated, and the code was not widely tested or implemented.

2.6 Improving the Computational Efficiency of Monte Carlo Simulations

Variance reduction methods are scenario-specific adjustments to a Monte Carlo simulation designed to reduce the number of randomly sampled particles that do not yield tallied data. The first method of variance reduction that is generally applied is known as geometry reduction. By eliminating regions of interactions that contribute negligible amounts of data to the output tallies, the computational efficiency is improved.

Another method of variance reduction is to reduce the relative importance of regions in which few interactions contribute to the output tally. For example, the wall of a room around a shielding experiment might be reduced to a hundredth of the rest of the simulation's importance. When a particle enters the wall, the simulation randomly determines whether it should continue to be tracked, or whether it should be "killed." In this case, the particle has a 99% chance of being killed. If it is not killed, the importance of this particle increases a hundredfold. This operation is known as "Russian Roulette." Should the particle then scatter and return to the inside of the room, it may be split into 100 identical particles, which is known as "particle splitting," or simply continue as a particle with 100 times the normal importance should it meet the simulation's tally criteria. Typically, an optimized Monte Carlo simulation will have a defined weighting window and apply Russian roulette and particle splitting to keep particle weights within a range of acceptable values.

Another approach to variance reduction is known as multi-step modeling. In this approach, a Monte Carlo simulation transports radiation to a surface of interest, tallying the particles that cross that surface. A subsequent simulation uses the flux spectrum crossing that surface as a source term. This method is of particular interest for radiation shielding and protection studies, since it allows an initial simulation to transport radiation from a source to a small region around the shielding, and then a series of subsequent simulations to evaluate different shielding scenarios.

Finally, it is possible to improve the computational efficiency of a Monte Carlo simulation by taking advantage of symmetries within the simulation similar to the assumptions driving the VCS program described earlier. For example, if a source is emitting radiation isotropically, and the wider environment does not vary considerably, then a radiation flux at one point from the source can be expected to be very similar at every equidistant point from the radiation source and other nearby surfaces such as the ground. This radial symmetry, when combined with multi-step modeling, can improve the computational efficiency of the overall approach by one to four orders of magnitude. Such an application is detailed in Chapter 3.

2.7 Validation Assessment Techniques

Unfolding the neutron spectrum from count rate measurements is done with the Maximum Entropy Deconvolution (MAXED) program. Using the measured count rates for each Bonner sphere measurement, an a priori spectrum from the MCNP6 simulation, and known Bonner sphere response functions, MAXED calculates an optimal neutron flux solution spectrum, f_i, which maximizes the entropy, S, as in

$$\boldsymbol{S = -\sum\left[f_i ln\left(\frac{f_i}{f^{DEF}}\right) + f^{DEF} - f_i\right]}, \quad (5)$$

Where $\boldsymbol{f^{DEF}}$ is the a priori spectrum. This produces a solution spectrum that matches the a priori spectrum while agreeing with the experimental count rates for each Bonner sphere measurement. MAXED also provides a validation metric in the form of a chi squared test by solving the resulting Lagrangian to produce a $\frac{\chi^2}{df}$ value. This value indicates a statistically significant result when it is less than one [77].

Assessing MCNP6's gamma radiation shielding accuracy is done by directly comparing ratios of dose information integrated from an MCNP6 pulse height tally and experimentally measured spectra. An F8 pulse height tally in MCNP counts the interactions within a simulated detector crystal and sorts these counts into predetermined energy bins [78]. The activity in each bin is multiplied by the energy associated with that bin, and the products are summed to produce a number representing the total dose. For a simulation using *m* bins, the resulting simulated gamma protection factor can be calculated as

$$\boldsymbol{GPF = \frac{Energy_{un}}{Energy_{sh}} = \frac{\sum_{i=1}^{m} E_i * A_{uni}}{\sum_{i=1}^{m} E_i * A_{shi}}}, \quad (6)$$

where $Energy_{un}$ represents the total energy deposited in the unshielded state, $Energy_{sh}$ represents the total energy deposited in the shielded state, *E* represents of the energy of the *ith* bin, and *A* represents the unshielded or shielded activity of each bin. Similarly, the experimental spectra can be numerically integrated, and the resulting unshielded energy absorbed is divided by the shielded energy absorbed.

Since dose is defined as energy absorbed divided by the mass of the absorbing body, the mass terms in both the shielded and unshielded scenarios cancel out when determining a GPF, the standard deviation for a GPF need not include the mass or dose of the absorbing body; the energy absorbed is sufficient. Since experimental spectra have three or more orders of magnitude higher count rates in their bins than their counterpart simulations, the statistical uncertainty of the experimental doses is negligible by the Law of Large Numbers. The MCNP6 simulation F8 pulse height tallies require post processing to evaluate. The activity in each bin is assumed to have a standard distribution by the Central Limit Theorem. MCNP6's F8 tallies include a quantity known as relative error, which is the standard deviation divided by the mean energy value of that bin. This means that low-activity bins tend to have high relative errors. The statistical error for these bins can be combined into a standard deviation for an energy measurement by Equation 7.

$$\boldsymbol{\sigma_{energy}} = \sqrt{\sum_{i=1}^{m}(\boldsymbol{E_i} * \boldsymbol{RE_i})^2} \tag{7}$$

In Equation 7, RE_i is the relative error for the *ith* bin. The resulting GPF standard deviation can be determined by Equation 8,

$$\boldsymbol{\sigma_{GPF}} = \sqrt{\left(\frac{\sigma_{unenergy}}{\boldsymbol{Energy_{un}}}\right)^2 + \left(\frac{\sigma_{shenergy}}{\boldsymbol{ENergy_{sh}}}\right)^2}, \tag{8}$$

Using this GPF standard deviation, a 95% confidence interval can be generated by taking the computed GPF and applying $\pm 2\sigma_{GPF}$. Comparing this 95% confidence interval to the experimental GPF provides a useful metric for the validity of the gamma radiation transport.

III. Methodology

3.1 The RPF Method

At its simplest, an RPF can be produced by simulations of a source environment with and without the presence of shielding. However, simulations alone are suspect; they may omit or improperly model factors affecting radiation transport. Therefore, most RPF evaluations used in this research involve three steps: a radiation shielding scenario experimentally measured with and without a shield, a MCNP6 model of the experimental measurements, and calculations of doses and the RPF. Due to the fact that neutron and gamma detectors used in this research have disparate geometries, an experimentally validated RPF requires an additional step of merging simulation geometries as shown in Figure 4.

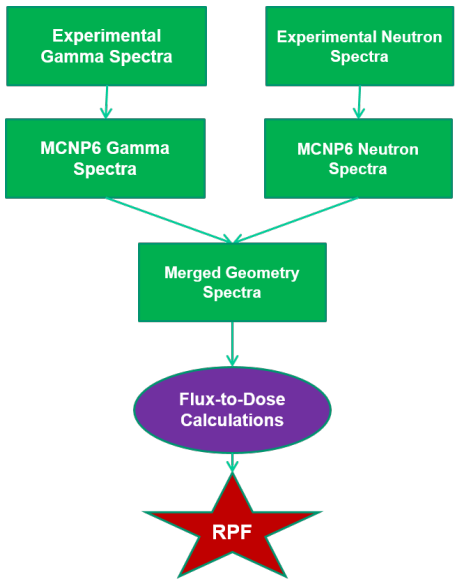

Figure 4. One method for producing experimentally-validated RPFs. In this case, experimental spectra validate particle transport, and then the modeled detector geometries are altered to match.

In this method, the models of gamma and neutron simulations are validated and then adjusted such that they share target geometry; a final pair of simulations then tally the gamma and neutron flux into this shared target in unshielded and shielded scenarios, doses are tallied, and the RPF is computed.

These steps varied depending on the scenario and radiation transport modeled. For short-distance irradiations with two feet or less between source and detector, radiation was transported from the source through the scenario's geometry to the detector in a single step. Modeling such scenarios required four simulations, consisting of gamma and neutron simulations with and without a shield. For irradiations with 12 feet or more between the source and detector, geometrically greater computing requirements required multi-step modeling approaches. One such approach is shown in Figure 5. More specifics about the multi-step approaches used in this research appear later in this chapter.

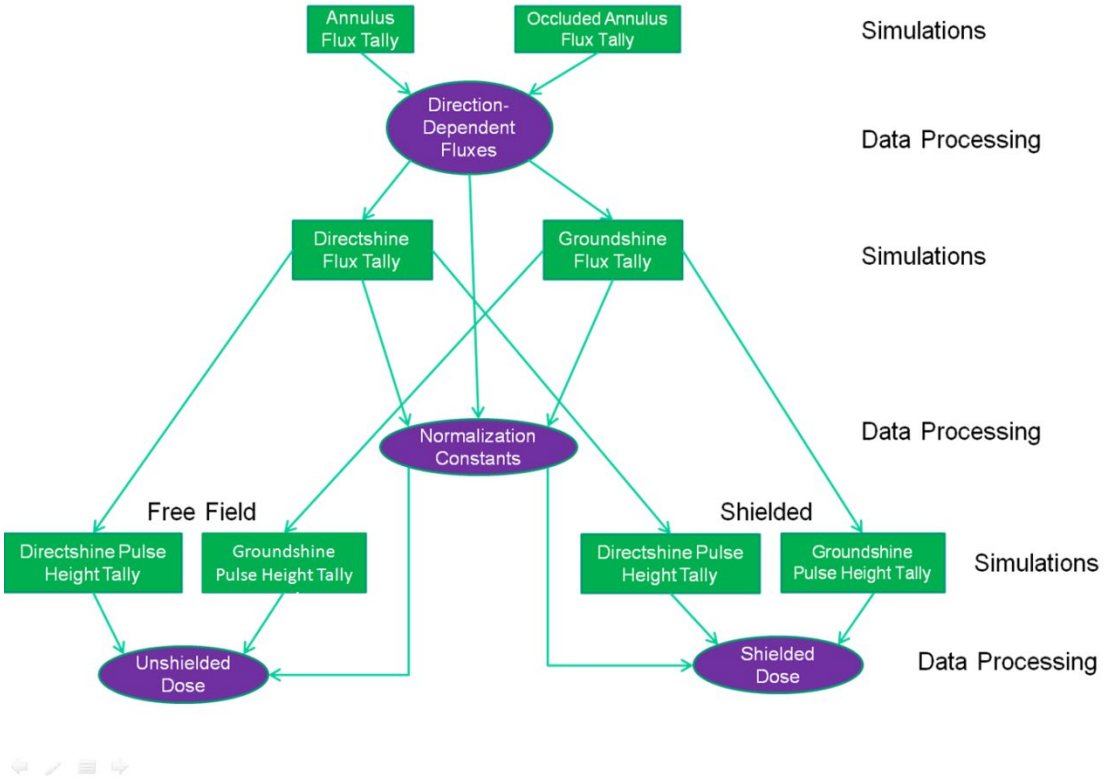

Figure 5. Steps for producing shielded and unshielded gamma radiation doses of a Fast Burst Reactor shielding scenario using a multi-step approach.

Different RPF calculation methodologies are explored, explained, and compared in further detail in Chapter 6.

3.2 Approach to Model Validation

This dissertation presents an iterative approach to developing the RPF methodology. Each subsequent chapter details a step meant to build confidence in the validation of MCNP6 as a platform for evaluating RPFs. The research that went into the experimental validation chapters was intended to evaluate the software and experimental equipment in scenarios of incrementally increasing difficulty and complexity. Each

chapter's research is meant to be mutually supporting without depending on a specific result to move from one chapter's content to the next.

The neutron detector used for experimental validation is the Ludlum 4 mm x 4 mm LiI scintillator [79]. The LiI detector is a thermal neutron detector and has almost no capture cross section for fast neutrons. Therefore, in order to get a neutron energy spectrum, this detector is used in conjunction with a set of Bonner balls consisting of high-density polyethylene spheres of varying diameter, which serve to thermalize a neutron flux to varying degrees. A full set of Bonner Balls is depicted with a LiI scintillator in Figure 6. By taking time-normalized count rates with the same detector in the same location with the same irradiating source, but with a different moderating thickness around the detector, it is possible to unfold a neutron spectrum using MAXED that is suitable for dose calculations [34, 80].

Figure 6. Complete Bonner sphere set with LiI scintillator. The active portion of the detector is inserted into the top pictured ball.

The gamma detector used in this research is the Saint Gobain BrilLanCe 380 ¾ in x 2 in LaBr scintillator [81]. This LaBr scintillator directly measures a gamma spectrum in a single measurement. The scintillating crystal of the LaBr detector is of similar shape and size to that of the LiI detector.

3.3 Experimental Validation with the PuBe Source

The first experimental validation study presented in Chapter 4 used a PuBe source for both neutron and gamma radiation. Its inactive training surrogate is pictured in Figure 7.

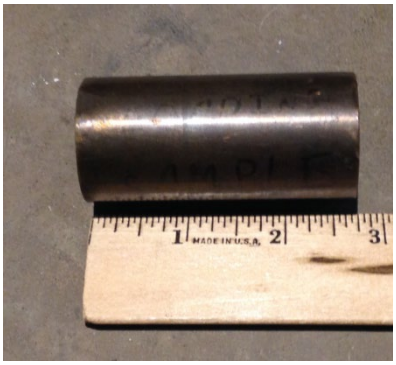

Figure 7. PuBe training surrogate with an identical size and shape, and a similar weight, to the active PuBe source.

This source represented a step up in complexity over monoenergetic radioisotope sources used in previous and parallel research described in Chapter 1. Unlike most single radioisotope sources, PuBe sources emit a probabilistic distribution of high-energy photons, as well as a probabilistic distribution of neutrons. This source irradiated detectors placed with and without a complex materials surrogate shielding enclosure pictured in Figure 8.

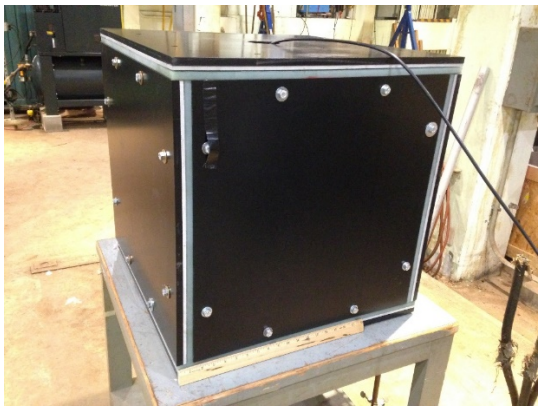

Figure 8. The complex materials surrogate assembled.

The shielding enclosure used in the PuBe evaluation was a 2ft x 2ft x 2ft box consisting of an 80/20 aluminum box frame with 22 inch sides covered by three layers of plates: a ½ inch steel layer, a ½ inch polyethylene layer, and a ¼ inch aluminum layer. This was meant to model different materials commonly used in military vehicle armor. The addition of the hydrogenous polyethylene layer added additional neutron moderation to the shielding.

3.4 Measuring the Gamma Emissions of the Fast Burst Reactor

The next validation experiment was meant to demonstrate MCNP's ability to model RPFs with energy spectra similar to those of a fission-only nuclear burst. While the Fast Burst Reactor (FBR) could provide such spectra, this presented a problem for experimental RPF assessments, because the gamma spectrum of the active FBR had never been directly measured before. The high fluxes of gamma radiation in the reactor chamber during operation had saturated all direct spectra measurements in previous attempts. Even after overcoming this challenge, the reactor's dynamic geometry between its active and shutdown state introduced spectral anomalies that prevented separating the residual decay

radiation of the reactor from its active output due to ongoing fission during operation. Chapter 5 details a novel approach that overcame these challenges by running the reactor at very low power, using attenuating sheaths around the gamma detector, and altering the reactor's shutdown procedure.

3.5 GPF Validation

The usable gamma spectroscopy techniques pioneered in Chapter 5 enabled a follow-on effort to validate MCNP6's ability to model gamma shielding benefits against the FBR's gamma emissions using a previously un-validated source term provided by the FBR team at White Sands Missile Range. This effort yielded negative results, and validation was not achieved after three attempts to adjust the models to better fit the data. Chapter 6 describes the efforts to recreate FBR gamma measurements and GPFs in MCNP6.

GPF validations used a similar enclosure to that of Chapter 4, replacing the aluminum and polyethylene composite plates with steel plates, as shown in Figure 9. This surrogate had already provided the preliminary scenarios for gamma and neutron transport validation at AFIT using a PuBe source, a Deuterium-Deuterium (D-D) neutron generator, and the FBR by Andrew Decker [34]. It was also evaluated for gamma transport in separate experiments using a ^{137}Cs source, a ^{60}Co source, and the FBR [35].

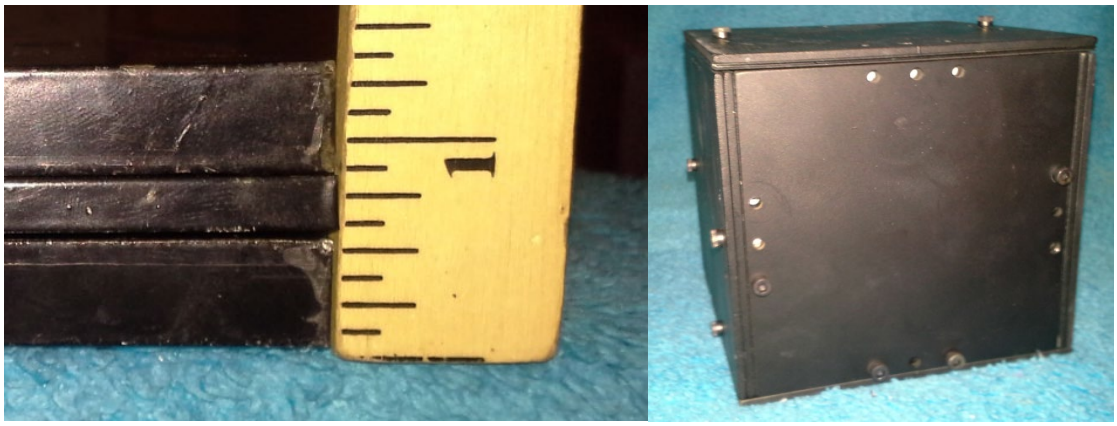

Figure 9. Steel plates used in the GPF outer shield, and a model of the assembled steel outer shield.

A third surrogate actually consisted of two surrogates. The first was a smaller version of the cubic simple steel surrogate built on a smaller 16-inch frame shown in Figure 10. This smaller steel enclosure was placed inside the larger steel enclosure. This configuration was intended to simulate a more complex geometry analogous to multiple compartments or layers in the same vehicle.

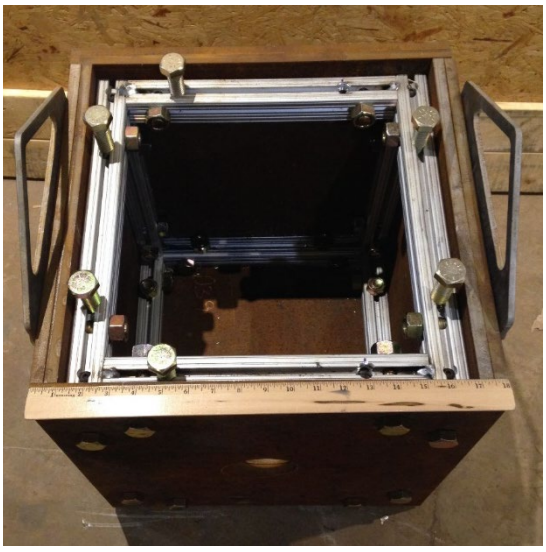

Figure 10. Inner enclosure used in the GPF evaluations.

3.6 RPF Techniques

Chapter 6 also describes and compares methods and strategies for modeling and calculating RPFs. Rather than experimentally validating the models, this section only uses MCNP6 models, examining the effects and utility of different tally techniques, target/detector geometries, dose calculation methods, and dose units upon RPFs. Practical factors considered include modeling efficiency, interest in stochastic vs. deterministic effects, variations in RPFs produced, and which approaches best fit the "most conservative" principle applied in radiation safety regulations.

3.7 Stryker Modeling

Finally, Chapter 6 describes a series of simulations modeling a Stryker vehicle subjected to the radiation field from a nuclear weapon. These models were assembled in SWORD and run in MCNP6. This effort was intended to evaluate a high-fidelity model of the vehicle and compare it to a steel right parallel-piped of similar dimensions and hull thickness to the Stryker. Comparing the RPFs produced at various angles to the modeled vehicle was intended to demonstrated the role of vehicle orientation with respect to a radiation source. Comparing the results of the high and low fidelity models would illustrate the importance of model fidelity and suggest what level of detail was required to achieve useful results. This modeling effort was ultimately unsuccessful for reasons discussed in Chapter 6.

3.8 Modeling Methodologies

For simulating PuBe irradiations of the steel and three-material surrogates, it is not necessary to do much variance reduction, as the distances involved are short enough that

the tally efficiency of the simulation is acceptable. Nor is it strictly necessary to use SWORD to produce the simulation, as the geometries involved are simple.

FBR simulations are far less computationally efficient to model due to the larger 8-12 ft distances between source and target and the geometrically greater volumes involved. While traditional weight window techniques of Russian roulette and particle splitting can result in some improvement, a more effective approach is multi-step modeling. In this approach, MCNP6 can use one simulation to transport radiation from the source to a region in the vicinity of the target and record the individually modeled particles as they cross into the region around the target. A subsequent simulation can model transport in and around the target itself. For the purposes of RPF simulations, a single simulation can model the radiation transport up to just outside a shielding enclosure, and subsequent simulations can model the radiation transport with and without shielding, with or without Bonner spheres of different radii, and with different types of detectors and tallies. Using this multi-step modeling approach, and keeping the second-step simulation volumes as small as possible, reduced the total simulation time for each RPF evaluation of the FBR by 72%.

In practice, this approach can be performed using the surface source write (SSW) and surface source read (SSR) cards in MCNP6, and this approach was used in some early GPF assessments of the FBR. Alternately, surface tallies from one simulation can define the source term for a second simulation or series of simulations; this was used in the majority of GPF assessments of the FBR and all of the later nuclear attack simulations using the Annulus Approximation described in the next section. The advantage of SSR and SSW cards is that they preserve the vectors of incident particles. The advantage of using

surface tallies is that they require smaller amounts of RAM and do not require the tallied geometry of the first simulation to match the source geometry of the second simulation.

Simulations of a nuclear explosion scale the problem up even further, since the distance at which an armored vehicle might endure a nuclear explosion far exceeds the inches to feet of the experiments in this research. This was important for initial assessments of the FBR, as well as Chapter 6's treatment of a nuclear weapon as a source term. Transporting radiation from that source over a kilometer or more required a method that could reduce computation time by more than two orders of magnitude.

The Annulus Approximation

Given an isotropic source in a large, open area, the flux across the surface of any detector equidistant from that source should be identical. Therefore, rather than tallying the interactions or fluxes going into LiI detectors twelve feet away from a simulated FBR, it is three orders of magnitude more efficient to revolve the volumes of those detectors about the simulated FBR, forming an annulus, and tally the flux into that annulus in a "step 1" simulation. Then, using the energy spectrum of that flux as a source term, a "step 2" simulation consisting of only the detector can produce simulated interaction data within the detector, as shown in Figure 11.

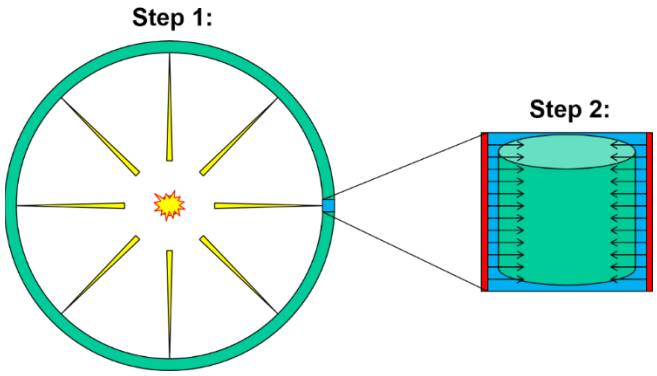

Figure 11. A representation of the annulus approximation applied to a simple two-step MCNP6 simulation.

The step 2 simulation can be expanded to model a shielding scenario as well. This approach, however, presents a problem for modeling shielding scenarios, as it loses directionally-dependent spectral information around the shielding geometry and detector in the step 2 simulations. Direction-dependent spectra are important, as many vehicles present more shielding at certain angles of incident radiation flux than to others. When neutrons and high-energy photons scatter off the ground and up towards a target, their energy is reduced, which changes the shape of the spectrum coming from that direction. In the parlance of nuclear weapons testing, this is referred to as ground-shine. Similarly, particles that scatter off the air and down toward a target are collectively referred to as sky-shine [75]. Both of these terms have become widely used in other radiation transport problems. For the purposes of this research, the term "direct-shine" is an appropriate addition to these terms. All three terms are shown schematically in Figure 12.

In order to account for these direction-dependent spectra at the FBR, the annulus simulation is modified, adding a second "killer" annulus inside the tally annulus. This killer annulus kills all particles that enter it, effectively eliminating direct-shine. Both the FBR

and the detector are placed approximately equidistant from the floor and the ceiling, and both the floor and ceiling of the FBR chamber are made of concrete. Therefore, for indoor FBR irradiations, no further direction-killing annuli are necessary, because the spectrum scattering off the ceiling of the reactor chamber is essentially identical to that scattering off the floor. For an outdoor FBR irradiation, a second killer annulus would also be necessary in order to isolate all three direction-dependent spectra. Depending on the degree to which spectral shape changes with incidence angle, more solid angles could be defined by adding and replacing additional killer annuli, but for the purposes of this research, two or three zones is an adequate approximation.

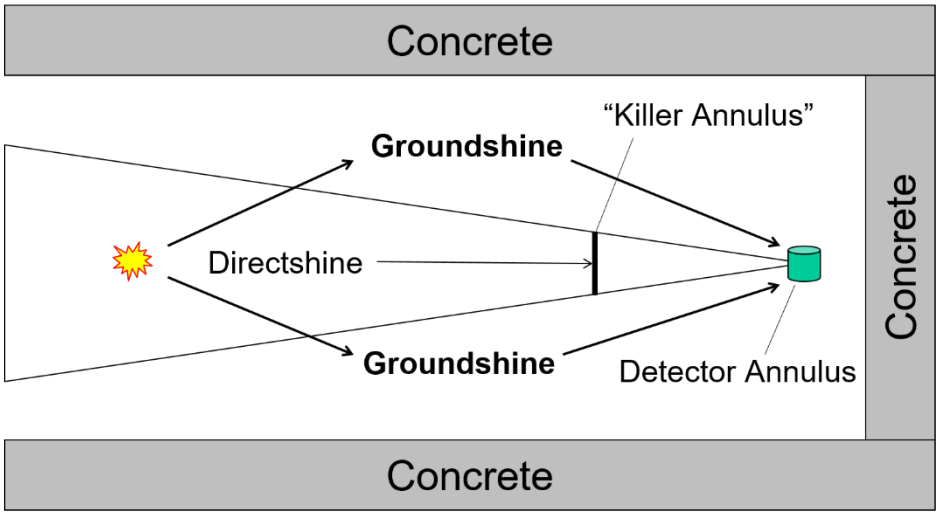

Figure 12. A representation of the method used to collect two direction-dependent flux spectra incident upon a detector-representing annulus.

These direction-dependent spectra must then be generated in a subsequent step 2 simulation that includes the radiation shield and the detector. The direct-shine spectrum is emitted by a flat surface source, while ground-shine and sky-shine are emitted by solid

angles of a cylindrical surface source with its central axis passing through the detector, as shown in Figure 13.

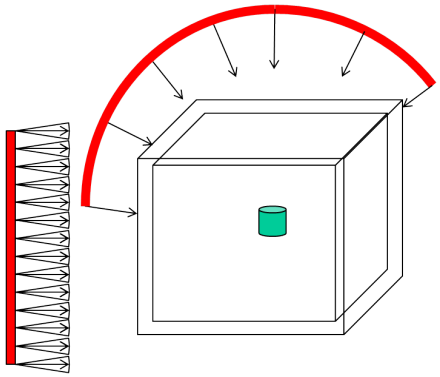

Figure 13. Representation of applying the direct-shine and ground-shine spectra to the shielding enclosure and detector in the second step of a directionally-dependent annulus approximating two-step MCNP6 simulation.

IV. Development of Radiation Protection Factors with Gamma and Neutron Spectroscopy Using a Plutonium-Beryllium Source

This chapter was published as a paper in the Journal of Radiation Effects in April 2018: W.J. Erwin, E. Cazalas, J.W. McClory, A.W. Decker, "Development of Radiation Protection Factors with Gamma and Neutron Spectroscopy Using a Plutonium-Beryllium Source," *Journal of Radiation Effects, Research and Engineering*, vol. 36, no. 1, pp. 88-93, April 2018.

4.1 Abstract

Verification and validation of computational codes for radiation protection requires detailed understanding of model generation and results, and how these compare to the experimental design and measured data. This work explores the degree of protection offered by a shield against a source that contains both neutron and gamma radiation, known as a radiation protection factor. Neutron spectra are calculated using a flux spectrum unfolded from Bonner sphere spectroscopy, whereas the photon dose rate is calculated through gamma spectroscopy. This work focuses on photon dose contribution through comparison of the MCNP computed vs. the experimentally measured gamma protection factor values using the gamma spectrum emitted by a plutonium-beryllium source. Results show that the computational and experimental gamma protection factor values match within 3%, which is significant, and the primary sources of deviation are understood and described. Finally, a combined radiation protection factor from constituent gamma and neutron dose rates is calculated.

4.2 Introduction

During the Cold War, robust experimental testing quantified the degree of protection provided by military ground vehicles against the hazards of ionizing radiation to their crews and passengers. One of the most important products of these investigations was the establishment of the radiation protection factor (RPF), a number which allowed planners to accurately assess the nuclear survivability of mounted ground forces in a variety of scenarios [82]. Additionally, RPF evaluations informed vehicle crews how best to orient and configure their vehicles against radiation hazards prior to and during radiation exposure.

Although testing procedures and facilities for evaluating RPF data have atrophied since the Cold War, the improved computational capabilities available today allow these investigations to be conducted using the Monte Carlo N-Particle version 6 (MCNP6) physics simulator [83]. To validate the ability of MCNP6 to produce reliable RPF values, prior work was conducted to evaluate MCNP6 code, producing gamma protection factor (GPF) values [35, 34, 82, 84] and neutron protection factor (NPF) values [85, 86]. The focus of this research is to demonstrate the validity of using computational simulations to estimate experimental RPF values by 1) providing additional measurements of GPF and NPF values in mixed neutron/gamma radiation fields using a PuBe (plutonium-beryllium) source; 2) exploring the ability of MCNP code simulations to match experimental spectra despite the issues of pulse pileup; and 3) calculating the quantitative combination of NPF and GPF values into a combined RPF.

This method of matching experimental and simulated RPF values relies on the ability of MCNP6 to predict the interaction physics of radiation with shielding and with

objects enclosed in the shielding, in this case a detector. Accurate simulation requires detailed modeling of the experimental geometry, knowledge of the source emission, and normalization of tally results to the source strength.

Dosimetric information can be obtained from the simulation by flux-to-dose conversion, as performed for neutron dose, or by summing energy deposited into the detection region, as done herein, for gamma dose. The demonstration of matching experimental and simulated GPF values using a PuBe source further exhibits the capability to perform such matching in mixed gamma/neutron fields..

4.3 Background

An RPF is a unit-less ratio of the dose (D) or dose rate (Ḋ) in a free-field (FF) measurement to a measurement taken within a shielding enclosure (SH) in an otherwise identical radiation field. RPF values can be calculated from the dose rate as in Equation 9 [5].

$$\boldsymbol{RPF} = \frac{\dot{\boldsymbol{D}}_{\boldsymbol{FF}}}{\dot{\boldsymbol{D}}_{\boldsymbol{SH}}} \tag{9}$$

The RPF can be broken into constituent gamma and neutron dose rates as in Equation 10.

$$\boldsymbol{RPF} = \frac{\dot{\boldsymbol{D}}_{\boldsymbol{\gamma,FF}} + \dot{\boldsymbol{D}}_{\boldsymbol{n,FF}} + \dot{\boldsymbol{D}}_{\boldsymbol{(n,\gamma),FF}}}{\dot{\boldsymbol{D}}_{\boldsymbol{\gamma,SH}} + \dot{\boldsymbol{D}}_{\boldsymbol{n,SH}} + \dot{\boldsymbol{D}}_{\boldsymbol{(n,\gamma),SH}}} \tag{10}$$

Included in the RPF of Equation 10 is the dose contribution from neutron activation via (n,γ) decays. The (n,γ) dose contribution is not considered in this paper but will be explored in future work. It is expected that (n,γ) contribution to RPF value is small while

in an active radiation field. The NPF and GPF values are formed by the dose ratios in Equation 9 but for only neutrons or gammas, respectively.

The neutron-based experiments to measure NPF values consist of a series of measurements taken in a PuBe radiation field with a LiI (lithium iodide) detector using moderating Bonner spheres of various radii in both shielded and free-field arrangements. The measured neutron spectra can then be unfolded using Bonner sphere spectroscopy (BSS) utilizing the MAXED (Maximum Entropy Deconvolution) code [84]. The gamma-based experiments to measure GPF values consist of two sets of measurements with a LaBr (lanthanum bromide) detector in shielded and free-field setups.

Figure 14. The geometry of the MCNP model in air including the composition and thicknesses of shielding material, inner detector, and PuBe source. The geometry is to-scale for the experimental shielding setup excluding walls, ceiling, and floor. Geometry and material makeup of the PuBe source is included from specification sheets provided by the manufacturer (Monsanto Research Corporation).

The experimental shielded setup reproduced in MCNP6 is shown in Figure 14 for a gamma field measurement. For the free-field setup, shielding material makeup and density is set as surrounding air in the simulation.

In order to validate the ability of MCNP6 to produce reliable GPF estimates, an F8 pulse-height tally records the energy deposited by photon interactions within the simulated detector. Binned by energy, the simulated spectra are compared to experimental measurements. Since the detector's mass does not change and divides out in the GPF calculation, an actual calculation of dose is unnecessary and a representational Dose can be calculated by multiplying bin count by bin energy for both simulation and experiment. An F4 energy flux tally of photons into the simulated LiI detector can also be used to calculate dose if $(\mu/\rho)_{en}$ ratios (LaBr to tissue) are applied. However, given the primary goal of validating MCNP6 code's ability to replicate the experiment, the F8 tally was, instead, utilized for dose and GPF comparison. For NPF value determination, a flux-to-dose conversion was used for the simulated results. Flux-to-dose conversion was necessary in the case of NPF determination due to the complicated nature of spectral deconvolution and recognizes neutron flux as a more analogous measure in a comparison between experiment and simulation.

4.4 Gamma Protection Factor Results

A 5 Ci PuBe source (provided and calibrated by Monsanto Research Corporation) produced the mixed neutron/gamma field with LiI and LaBr detectors for neutron and gamma measurements, respectively. Detectors were placed ~31 cm from the PuBe source. For a free-field measurement setup, detectors are placed in open air, approximately 1.2 m

above the ground. In a shielded setup, the detectors were then placed within a 62.2 cm^3 enclosure as in Figure 14.

The results of experiment and simulation are shown in Figure 15 and show a close match between the two up to 4.5 MeV. Although gamma rays above these energies may be produced by fissions within the PuBe source, these constitute a small minority of fission emissions, and fissions within the source happen at much lower rates than the reactions producing 4.5 MeV gamma rays; therefore, significant activities above this energy are not associated with established PuBe emission spectra [85]. Measurements taken with the source removed show no activity in this energy region, and the dead time divided by the live time for these measurements was 1%; pulse pileup is a function of this ratio [87]. This suggests that the higher-energy discrepancies are likely due to pulse pileup. Pulse pileup occurs when two photons deposit energy into the detector active region within the same pulse length measurement period (roughly defined by the detector dead-time).

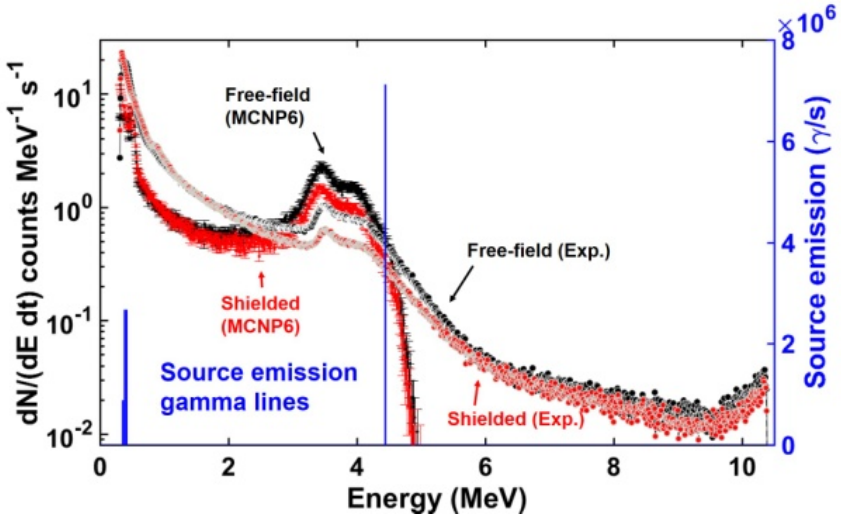

Figure 15. Comparison of experimental (Exp.) scintillation detector spectrum to MCNP6 simulation (MCNP6 with standard errors) with an F8 tally shows good matching of spectral features. Pulse pileup accounts for the discrepancy between experimental and simulated spectra above 4.43 MeV. Free-field measurements show higher count-rates in the Compton continuum of the 4.43 MeV source emission photon (right axis), as compared to shielded measurements, as expected due to shield attenuation. Error bars are included for all but the PuBe gamma source emission lines, which are shown for reference.

Pulse pileup and neutron interactions cause the extension of experimental spectra into energy regions higher than source emission line at 4.43 MeV. The MCNP6 code executed here does not calculate pulse pileup, the lack of which is shown at energies higher than ~5 MeV and in the energy region lower than ~2.5 MeV in Figure 15. However, this does not alter the dose contribution provided by the MCNP6 F8 tally as total energy is still deposited into the detector in the simulation. The simulation assumes the gamma line source emission in Figure 12 is created by the decay of the first and most probable excited nuclear state of the $^{12}C^*$ nucleus (4.43 MeV) created in the $^{9}Be(\alpha,n)^{12}C^*$ reaction [85]. Also included are the prevalent gamma decays (at lower energies) of ^{240}Pu and ^{241}Pu [86].

Figure 16 displays the experimental and MCNP6-derived GPF results. The extended plot of $GPF_{Exp.}$ at energies greater than ~5 MeV represents pulse pileup in the experiment.

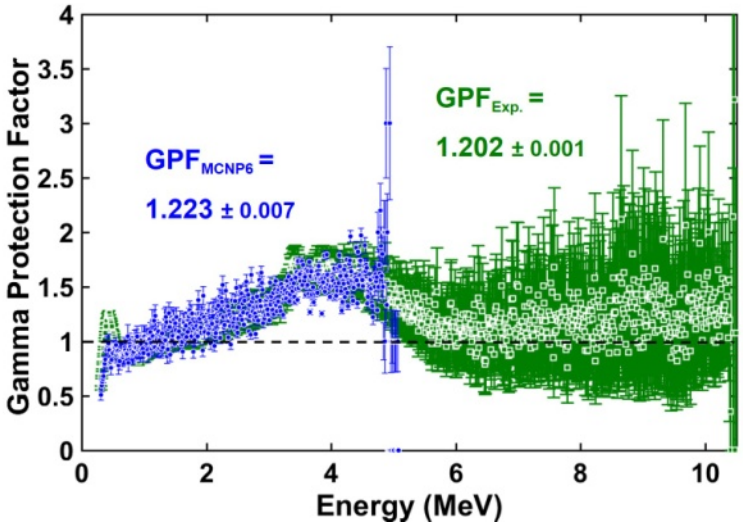

Figure 16. The overlaid gamma protection factors (GPFs) from MCNP simulation (GPF_{MCNP} in blue) and experiment ($GPF_{Exp.}$ in green) show good agreement up to 4.5 MeV. Error bars indicate standard error by bin. These standard error bars are calculated as the standard deviation of the photon energy deposited in each bin normalized to the energy of that bin. Standard deviations of the $GPF_{Exp.}$ at higher energies are larger due to low count rates of pulse pileup events. Above and below the dotted line, at GPF = 1, the shielding either reduces or increases the dose in the detector depending on the energy of the detected photons. Error bars are included in this figure.

Figure 16 shows that while the MCNP6 code did not include pulse pileup, GPF_{MCNP} matches $GPF_{Exp.}$ for energies up to 4.5 MeV. High energy contributions are still accounted for by the higher Compton continuums in the 4 MeV region in the simulation, as would be observed in a detector absent of pulse pileup. The large error bars of observations taken above these energies are caused by low detection rates in this region as shown in Figure 15. These low detection rates also mitigate the contributions of these higher energy bins to overall dose calculations and the associated experimental uncertainty. GPF results

displayed in Figure 15 are derived from the ratio of dose rates summed over the entire spectra, $\dot{D}_{FF}/\dot{D}_{SH}$. Figure 16 exhibits the importance of shielding against higher energy gammas (4.43 MeV) and the potential for producing lower energy Compton scattered photons (< ~1 MeV) due to shielding.

4.5 Neutron Protection Factor Results

Studies into the comparison of experimental and MCNP6 simulated setups have shown close agreement between NPF_{MCNP6} and $NPF_{Exp.}$ [88, 34]. Here, the NPF value is derived from an MCNP6 simulation using the experimental setup in Figure 14. Dose is calculated by extracting results from an F4:n flux tally. Dose is derived from a log-log interpolation of neutron flux-to-dose conversion tables provided in ICRP 74 [61].

Dose results, displayed in Figure 17, show that dose is imparted by both neutron absorption (at lower energies) and scattering (at higher energies). Figure 17 also shows that the shield had mediocre qualities for neutron dose reduction as exhibited in the NPF_{MCNP6}, which is qualitatively expected given the thickness and material makeup of the shield. Interestingly, the dose with shield is increased at lower energies (< ~1 MeV) due to neutron down-scattering and subsequent absorption. However, the larger flux of higher energy neutrons dominates the neutron protection factor as $NPF_{MCNP6} > 1$.

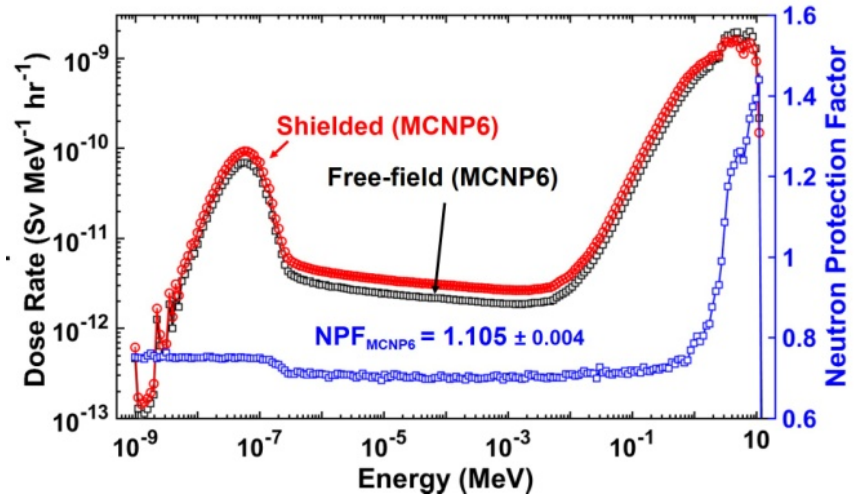

Figure 17. The neutron equivalent dose for free-field and shielded cases derived from the MCNP6 simulation of the experimental setup in Figure 11. The neutron protection factor (right axis) shows that presence of the shield actually increases dose for energies lower than ~1 MeV. Standard errors are included for all data but are smaller than the data points displayed.

4.6 Combined Radiation Protection Factor

The combined RPF value is an important metric of the dose reduction provided by a given shield in mixed gamma/neutron radiation fields. We calculate the RPF value with dose rates derived from the MCNP6 simulation of the experimental arrangement in Figure 17. The combined RPF is calculated using Equation 10 and results in an RPF = 1.187 ± 0.003. While it appears that the RPF value can be alternatively calculated by averaging the NPF and GPF values, this will only yield the correct RPF value if shielded neutron and gamma doses are the same or when the GPF and NPF values are the same.

4.7 Conclusion

This paper explores a new, simple, and experimentally verifiable method for determining RPF values of shielding geometries and materials, which has applications in

understanding mass-limited shielding effectiveness for military and civilian applications. For the specific scenario presented, a mixed neutron/gamma radiation field was examined using a PuBe source, providing additional verification of MCNP6 code's ability to accurately model shielding physics. Experimental and simulated GPF values are compared and it was shown that spectral discrepancy due to pulse pileup in the detector does not affect GPF value calculation. A simulated NPF was studied and the combination of gamma and neutron dose rates to calculate a combined RPF value from simulation was determined.

Future work includes additional validation of the MCNP6 code against experiment using other neutron and gamma sources, more complex shielding scenarios, and examining the contributions of neutron-activated gamma rays in the air and shielding around the target. These future studies will support research into more complex and dynamic scenarios, such as a nuclear burst, response to a nuclear or radiological accident, or some space radiation applications.

Acknowledgements

The authors would like to thank the Defense Threat Reduction Agency for its sponsorship and active support of this research, as well as Dr. James Petrosky and Mr. Eric Taylor for their assistance with handling the source for the experimental portion of this research.

V. The Gamma Emission Spectrum from the Fast Burst Reactor

This chapter was published as a paper in the Journal of Radiation Effects in April 2019: W.J. Erwin, E. Cazalas, A. Cahill, J.A. Clinton, J.W. McClory, A.W. Decker, "The Gamma Emission Spectrum from the Fast Burst Reactor," *Journal of Radiation Effects, Research and Engineering*, vol. 37, no. 1, pp. 50-56, April 2019.

5.1 Abstract

During operation, the Fast Burst Reactor (FBR) at White Sands Missile Range (WSMR) emits high photon fluxes that saturate spectrometers, thereby degrading gamma measurements. Additionally, the measured gamma spectrum during shutdown is substantially different from the gamma spectrum emitted during operation due to changes to reactor geometry during shutdown. Monte Carlo N-Particle (MCNP) simulations have characterized the FBR's prompt gamma spectrum, but this spectrum has not previously been experimentally verified and validated. In this research, three methods were employed to reduce scintillation detector saturation and dead time: using a smaller detector, operating the reactor at the lowest maintainable power, and using shielded spectrometers to reduce gamma fluxes. To reduce spectral differences in background radiation associated with the shutdown of the reactor, the shutdown procedures were altered, resulting in a shutdown state geometrically similar to the reactor's operational state. Measured operating spectra are compared to MCNP simulations of the prompt gamma emissions from the reactor and neutron-gamma interactions in the materials surrounding the detector.

5.2 Introduction

The Fast Burst Reactor (FBR) has been used for evaluating radiation effects from unmoderated fission sources. Spectroscopic techniques for evaluating the reactor's neutron flux have included neutron activation analysis and Bonner sphere spectroscopy. Although the neutron energy spectrum emitted by the FBR has been characterized by experimentation and modeling [82, 34, 88], the reactor's prompt gamma energy spectrum has generally only been characterized by modeling [38, 36, 89]. The shape of this prompt gamma spectrum is important for improving experimental designs, shielding considerations, accurate radiation modeling, and understanding and interpreting experimental results.

This research is an experimental investigation of the FBR's operating gamma output and a comparison between the experimental results and Monte Carlo N-Particle ver. 6 (MCNP6) simulations of the FBR's prompt gamma emission spectrum [83].

5.3 Background

As a bare metallic reactor with very high enrichment, the FBR is frequently used to approximate weapon-like energy distributions of ionizing radiation. As such, its gamma energy spectrum is important for understanding the effectiveness of shielding personnel against the prompt radiation from a nuclear burst. Understanding the energy distribution of gamma rays from a fission weapon is also important for modeling weapon effects. For instance, models of high altitude electromagnetic pulse use prompt gammas emitted by a nuclear burst as an input, and typically approximate this distribution to a single energy [90] [91] [92]. A validated prompt gamma spectrum could allow for a more realistic set of inputs

to such simulations. Finally, given NASA's interest in Kilo-power, a project creating reactors of similar composition and enrichment for deep space missions [93], understanding the operating gamma spectrum of a similar reactor is important for shielding personnel and equipment from the ionizing radiation of such reactors.

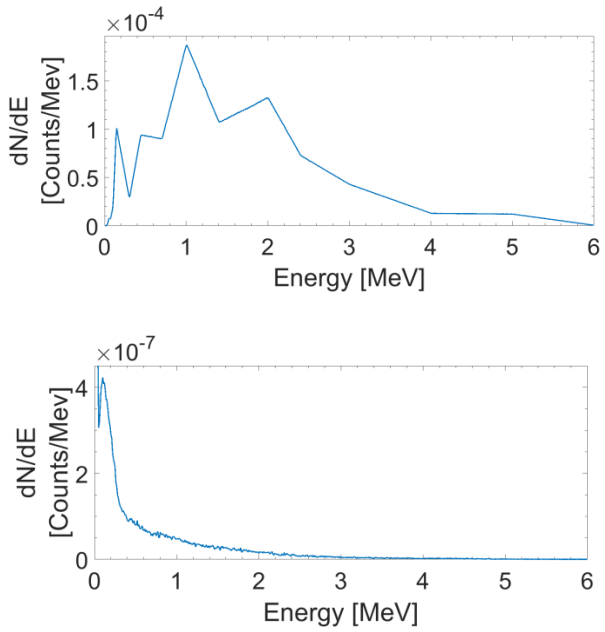

Figure 18 Top: MCNP5 tally of the prompt gamma flux spectrum across the surface of the FBR, recreated from data provided by the Survivability, Vulnerability & Assessment Directorate, WSMR. Bottom: MCNP pulse height tally from a simulation transporting the top spectrum into a small $LaBr_3$ detector. Uncertainties were $8.6 \cdot 10^{-9}$ counts/MeV-s or below for energys bin of both tallies.

The simulated prompt gamma emission spectrum from the surface of the FBR is shown in Figure 18, along with the results of a simulation transporting this spectrum into a scintillation detector. As shown in the bottom of Figure 18, high photon energies have low probabilities of full energy deposition. The detector modeled was a cylindrical $LaBr_3$ crystal with a radius of 0.75 inches and a length of 2 inches that modeled the device used in experimental measurements.

Gamma ray energy deposited in a detector during and immediately after FBR operation comes primarily from three sources: prompt gamma emissions from the reactor, neutron-gamma interactions in the environment, and fission product decay gamma emissions. The total gamma spectrum can be expressed as a summation of these constituents:

$$\boldsymbol{G_{Total} = G_{Prompt} + G_{n\gamma} + G_{Decay}.} \quad (11)$$

A rearrangement of this equation indicates the three components needed to produce an experimentally-derived basis for validating the modeled prompt gamma spectrum is

$$\boldsymbol{G_{Prompt} = G_{Total} - G_{n\gamma} - G_{Decay}.} \quad (12)$$

Determining each contributing component of Equation 12 entails unique challenges.

The high-flux radiation environment in the reactor chamber during operation results in large dead times and makes measuring G_{Total} difficult. Previous measurements of gamma spectra 12 feet from the FBR yielded dead-times of 100% (3 × 3 inch NaI, at 1 W reactor power) and 19.3% (0.75 × 2 inch $LaBr_3$, at 0.5 W reactor power).

Measuring G_{Decay} poses problems due to the dynamic geometry of the reactor's conventional shutdown procedure. Previous attempts to measure the gamma spectrum immediately after shutdown assumed that the reactor's output from decay radiation would be the same in its operational state as in its conventional shutdown state.

The FBR consists of three primary fuel components: a stack of rings, a central cylinder known as the "safety block," and three control rods. All three fuel components are enriched to over 90% ^{235}U. These components are configured as shown in Figure 19. When operating, the safety block is fully inserted and control rods are partially inserted to regulate

the power of the reactor. The standard shutdown procedure is to lower the safety block out of the center of the reactor, bringing the assembly to a subcritical state and quickly halting the neutron chain reaction. Previous efforts to measure the prompt gamma spectrum of the FBR have been attempted by taking a spectrum with the reactor operating and then taking another spectrum immediately after shutdown.

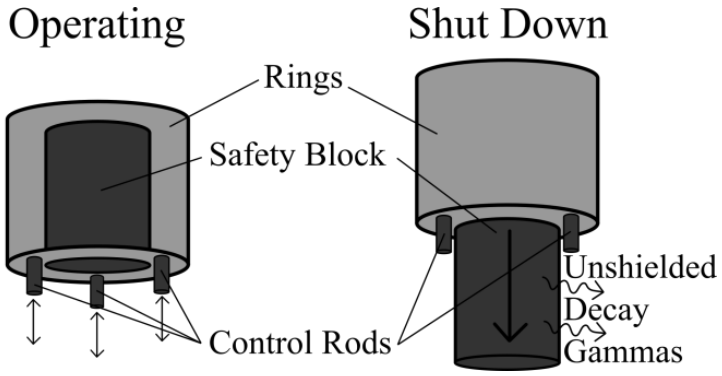

Figure 19. A simplified diagram of the FBR fuel elements in operating and shut down geometries.

This approach yielded spectral features due to the dynamic geometry of the FBR. Because of its central location within a reactor of uniform enrichment, the neutron flux and density of fissions is highest inside the safety block. Therefore, the highest concentration of fission fragments and their daughter products is found in the safety block. When the reactor shuts down, the act of lowering the safety block exposes these higher concentrations of radioactive isotopes that are shielded by the rings during operation. Gamma rays from longer-lived isotopes such as ^{137}Cs are therefore more prominent in the reactor chamber with the reactor shut down than when the reactor is operating. This results in the spectral features in the prompt gamma spectrum shown in Figure 20, which displays an approximation of G_{Prompt} as $G_{Total} - G_{Decay}$. For the purposes of this research, this is

called an "operating gamma spectrum" or "experimental prompt gamma spectrum," although it includes some decay gammas associated with the time required for reactor shutdown, and should not be confused with a true prompt gamma spectrum, which is generally limited to emissions happening within a microsecond of an individual fission.

Gamma rays from neutron interactions outside the reactor are not included in the prompt gamma emission spectrum from reactor simulations, as they depend upon the geometry and materials in the reactor's environment which vary from experiment to experiment. While $G_{n\gamma}$ is difficult to experimentally isolate from the prompt gamma emissions, it can be approximated using MCNP6 simulations combined with experimental neutron measurements of the reactor.

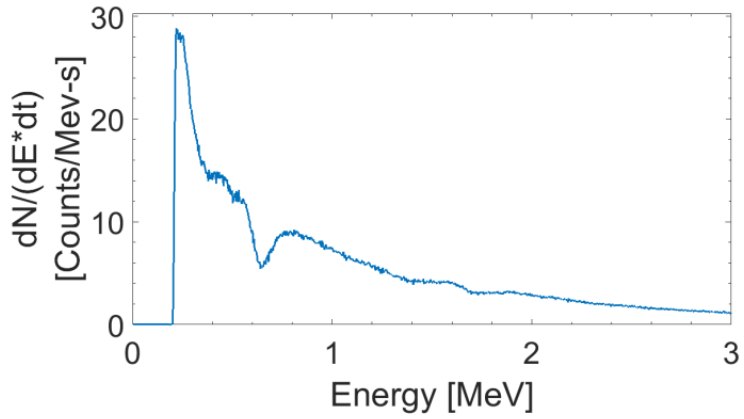

Figure 20. A measurement of the prompt gamma rays produced by the FBR. This was created by subtracting the spectrum taken immediately after a standard shutdown from the spectrum taken while the reactor operated at a steady state of 500 mW. Note the large spectral drop around 0.66 MeV and two minor spectral drops between 1 and 2 MeV. These drops are due to the subtraction of the more prominent emissions of ^{137}Cs and ^{60}Co in the shutdown geometry. Uncertainties were $1.3 \cdot 10^0$ counts/MeV-s or below for each energy bin.

These are the dominant contributors to the gamma flux in the reactor chamber during operations, but they are not the only sources. However, experimental background

measurements of the reactor chamber with the reactor removed to its storage bay showed approximately four orders of magnitude less activity than what was detected during reactor operation and shutdown measurements, and is therefore not considered significant for the purposes of this research.

5.4 Methodology

In order to reduce the flux of the G_{Prompt} experimental measurement, the reactor was configured to run at 250 mW, its lowest sustainable level. Unfortunately, circumstances of a concurrent experiment forced the placement of the detector slightly closer to the reactor, which resulted in a similar flux of gamma rays into the detector to those of previous measurement attempts.

To further reduce dead-time in the scintillation detector, a series of tungsten sheaths was machined to fit tightly around the $LaBr_3$ crystal. These sheaths had thicknesses of 1, 2, and 4 mm. Spectra were collected with the bare detector and each attenuating sheath. This was intended to reduce the flux of lower-energy gamma rays within the detector and reduce the dead-time of these measurements by varying degrees, thus improving the quality of the G_{Prompt} measurement.

In order to eliminate the spectral features associated with previous efforts to measure G_{Decay}, the reactor's shutdown procedure was altered. Rather than dropping out the safety block as in a conventional scram, the control rods were withdrawn to bring the FBR to a subcritical state. While this change lengthened the FBR shutdown time from less than 1 second to 30 seconds, this altered procedure resulted in a shutdown geometry that was similar to the operating state for the purposes of shielding the safety block.

The simulated gamma emission spectrum of the FBR was used as an isotropic point source in a multi-step MCNP6 simulation of the reactor chamber. The gamma flux was tallied entering a representative cell that enclosed a volume around the detector in an initial simulation; this tally became the source term for simulating the detector and its tungsten sheaths in subsequent simulations.

While the prompt gamma output of the reactor has not been experimentally validated, the neutron spectrum of the reactor has been thoroughly investigated and validated [47, 88]. MCNP6 simulations transported this validated neutron spectrum and tallied the $G_{n\gamma}$ term, which was normalized using neutron measurements of the reactor. A second series of simulations replaced the FBR's gamma emission spectrum with its neutron emission spectrum and neutron-gamma interactions in the environment were tracked. Both neutrons and gamma rays were tallied entering a cell enclosing the detector and the air within 12 inches of the detector in an initial simulation. This tally became the source term for simulating the detector and its tungsten sheaths. The yielded tallies of gamma interactions in the detector were solely due to neutron interactions in the environment.

MCNP6 tallies are normalized to the number of source particles in the simulation. Thus, a simple multiplication of the neutron-gamma simulation tallies by the neutron emission rate of the reactor yielded an approximation of the time-normalized neutron-gamma spectrum ($G_{n\gamma}$). Since the power-dependent prompt gamma emission rate is not well-defined, the MCNP6 prompt gamma tally's normalization constant was optimized to produce a best fit to the experimental data.

Validation of the prompt gamma spectrum was initially done by direct comparison of the experimentally-derived prompt gamma spectrum of the detector to an MCNP6-

modeled transport of the reactor prompt gamma source spectrum into the simulated detector. This was accomplished by visual inspection of both spectra and by comparing the relative proportions of key points in their spectra. The energies of these points were specifically selected to represent regions of dominance for photoelectric absorption, Compton scattering, and pair production.

An unplanned benefit of using the tungsten sheaths was that each sheath thickness provided an additional point of comparison between the MCNP6 model and measured spectra. Comparing the attenuation of these models and experiments across the simulated and experimental spectra provided a basis for validating the higher-energy portion of the prompt emission spectrum than would otherwise have been possible. Since the tungsten sheaths were denser than the detector crystal, they could produce significant differences in count rates of photon energies up to 3 MeV, and due to the attenuation of lower-energy photons, the lower portion of the thickly-shielded detectors could be attributed to pair production and scattering of higher-energy photons.

A pulse pileup algorithm was created in MATLAB and applied to modeled spectra to enable a direct comparison between experimental results and model outputs. This algorithm consisted of four key steps. First, the algorithm randomly sampled time intervals between successive pulses based on the detection rate associated with that experimental spectrum until the combined time interval exceeded the per-event dead time of the detection system's multi-channel buffer. Second, the algorithm sampled energies for each of these pulses. Third, a Gaussian distribution was applied to each pulse over the time interval as a function of time, according to the measured pulse shape and width in the detection system. These Gaussian pulses were summed over the interval, effectively

simulating a snapshot of an oscilloscope window connected to the detection system. Finally, the algorithm would find and report the first peak, while ignoring all subsequent peaks, similar to a multichannel buffer. This algorithm would then be repeated to construct a simulated spectrum that accounted for the effects of pulse pileup.

5.5 Experimental Results

Both the reduction in reactor power and the use of tungsten sheaths reduced experimental dead times to varying degrees as shown in Table 2. While the residual presence of dead times from 8% to 18% from decay gammas could be reduced with a fresh fuel load or by scheduling this experiment after a lengthy period of inactivity for the reactor, this was not feasible for the purposes of this experiment.

Table 2. Dead-time percentages for each experimental observation. Shutdown dead-times are of the reactor in its modified shutdown state with the safety block still inside.

	Dead-Time [%]			
Operating Power	No Sheath	1 mm	2 mm	4 mm
500 mW	**37.1%**	**25.3%**	**26.6%**	**23.3%**
250 mW	**25.9%**	**17.4%**	**15.7%**	**14.3%**
Shutdown	**18.0%**	**11.5%**	**10.7%**	**8.3%**

The experimental prompt gamma spectra collected lacked the spectral features seen in earlier efforts to measure the operating gamma output of the FBR, as shown in Figure 21. This is consistent with the hypothesis that these anomalies were due to reduced shielding of the fission fragment gamma rays in the safety block in the FBR's standard shutdown. Thicker tungsten sleeves caused lower detected activities, particularly at lower

energies. This is consistent with the lower activity and dead times of these observations and well-known theory of high-energy photon flux attenuation through shielding media. The modeled prompt gamma spectra shared a similar overall shape with their experimental counterparts.

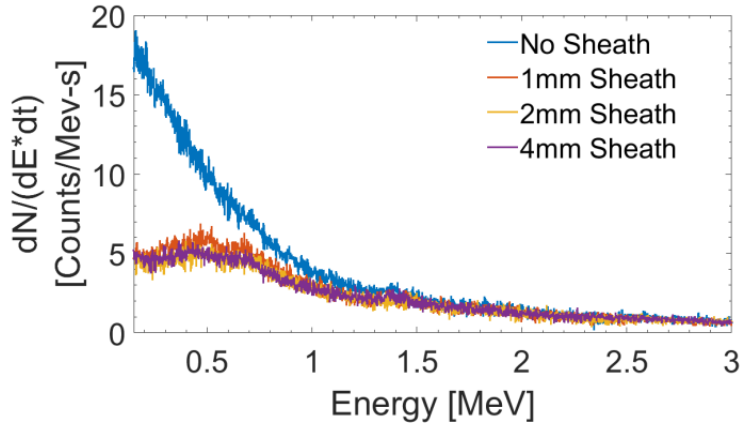

Figure 21. A comparison of prompt gamma spectra from the FBR measured with different sheath thicknesses. Each spectrum was produced by subtracting the modified shutdown spectrum from a spectrum taken during 250 mW steady state operation. Uncertainties were $1.1 \cdot 10^{0}$ counts/MeV-s or below for all spectra displayed.

5.6 Dead Time Reduction

Dead time reduction was successful to varying degrees depending on the reactor power level and the presence and thickness of a tungsten sleeve, as shown in Table 2. While operating the reactor at lower power helped to minimize dead-times, the shutdown state radiation of the reactor could not be effectively reduced within the experimental timeframe. Thus, even with the reactor shut down, the bare detector still showed significant dead time that required tungsten sheath attenuation for further reduction.

Additionally, while previous measurements of the prompt gamma spectrum indicated a high level of lower-energy gamma rays, much of this lower-energy activity in

the detector was revealed to be from high-energy gamma rays undergoing Compton scatter inside the detector. This is demonstrated in Figure 21, which shows a significant decrease in detected photons less than 1 MeV when tungsten sheaths of any thickness are used. Smaller decreases are measured with decreasing thicknesses of the tungsten sheaths. This is consistent with the dead times reported in Table 2, where one millimeter of tungsten reduced the dead times by approximately 30%, while a sheath four times thicker reduced the dead times by 40%.

5.7 Modeling the Prompt Gamma Spectrum

The three strategies employed in MCNP6 and post-processing yielded spectra similar to the experimental prompt gamma spectra as shown in Figure 22. The two-step modeling approach reduced the computational requirements of the simulations by 71%, eliminating the need to repeat the initial simulation for each of the four simulated spectra. The built-in Gaussian broadening feature in MCNP modeled spectral peak broadening due to detector resolution.

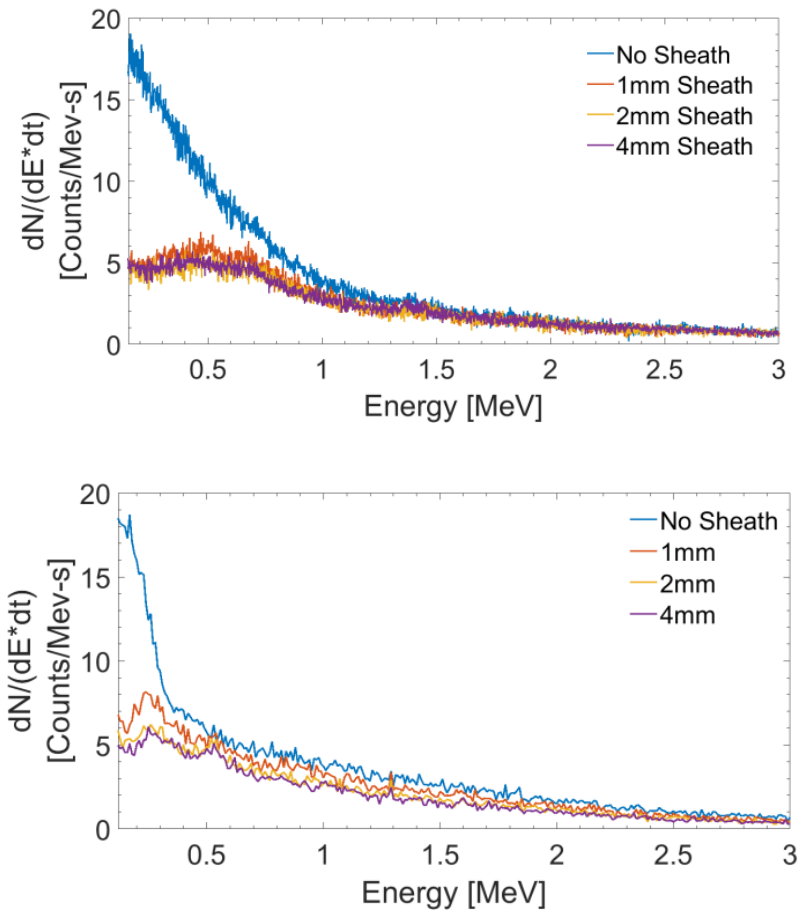

Figure 22. Comparison of experimental spectra (top) and modeled spectra (bottom). Uncertainties were $1.1 \cdot 10^{0}$ counts/MeV-s or below for the experimental spectra and $4.3 \cdot 10^{-1}$ counts/MeV-s or below for the modeled spectra.

While the shapes of the spectra in Figure 22 are similar, a close examination shows one major difference. The experimental bare detector plot shows noticeably higher count rates than the measurements taken with tungsten sheaths at energies below ~1 MeV. In the modeled spectra, this difference is noticeable just under ~0.5 MeV and rises more sharply as the energy of the interaction decreases. This difference, as well as other, smaller differences between the modeled and experimental spectra, may be attributable to two sources of experimental gamma emissions that are not included in the prompt gamma

model: neutron-gamma interactions and fission fragment products which decay in significant proportions between the measurement taken with the reactor operating and the end of the measurement taken after shutdown.

5.8 N-Gamma Simulations

The n-gamma simulations yielded spectra dramatically different from the experimental measurements. As shown in Figure 23, the simulated n-gamma spectra of the sheathed detectors yielded significantly more gamma interactions than the bare detector n-gamma simulation. Neutron interactions in the tungsten sheaths create more n-gamma interactions than air, and as the sheath gets thicker, the n-gamma contribution grows.

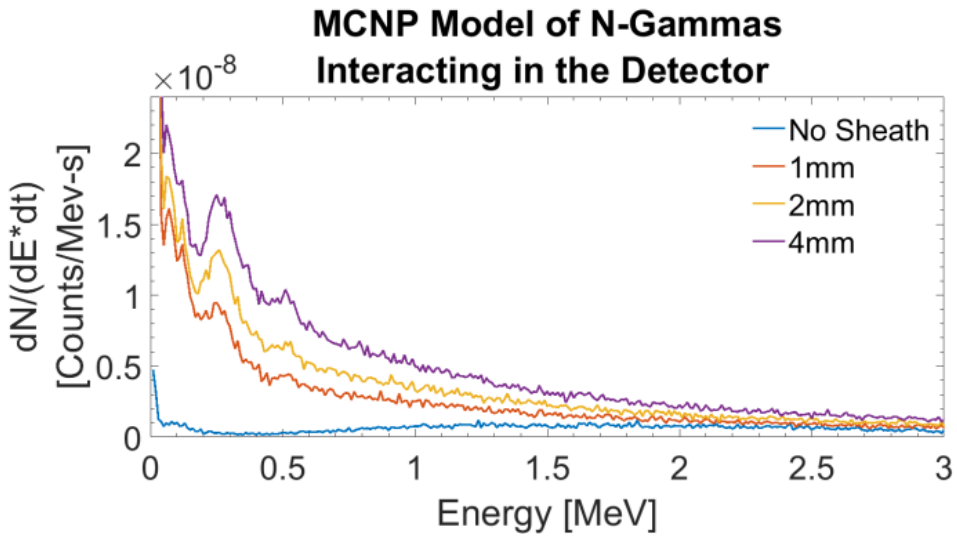

Figure 23. Simulated gamma spectra in the detector resulting from n-gamma interactions. Uncertainties for these spectra were $1.6 \cdot 10^{-9}$ keV/kg-or below.

The inversion of the observed experimental spectra, as a function of sheath thickness, is consistent with n-gamma interactions being a small minority contributor to the overall experimental prompt gamma spectrum measured. Accurately combining the n-

gamma spectrum with the prompt is impractical, as the n-gamma simulations are normalized to the number of source neutrons, while the prompt gamma spectrum provided was not, and the simulation that produced the prompt gamma emission spectrum is not available. The particularly low contribution of n-gammas under 1 MeV in the unshielded spectrum indicates that n-gamma contributions do not account for the noticeable discrepancy between the bare modeled spectrum and its experimental counterpart. Thus applying any normalizing constant to the n-gamma spectra and adding it to the prompt gamma spectra does not yield a better fit to the experimental data, and makes the comparison worse if the n-gamma contribution is more than two orders of magnitude smaller than the prompt gamma contribution. This source of gamma rays is therefore not a significant contributor to the total gamma spectrum measured.

5.9 Short-Term Decay Gammas

Due to both the modified shutdown procedure and the need to collect sufficient counting statistics in the experimental post-shutdown spectra, the experimental decay spectrum was measured for approximately 2 minutes once the operational spectrum measurement ended. The MCNP model of the FBR's prompt gamma output models gammas produced within about a microsecond of fission. Thus any radioactive nuclei produced by fissions that decay away more than 10% within those 2 minutes are not included in the prompt gamma simulations. Measurements of post-fission spectra over time have been the subject of several studies [94, 95, 96]. Since these spectra are of other reactors, these measurements are of limited quantitative utility in this work, but can be qualitatively studied to show the importance of shorter-lived decay gammas. Evaluations

of short-lived gamma data suggest high gamma ray detection fluxes in the ~0.5 to ~1.5 MeV range at 128 seconds after ^{235}U fissions [94, 95], which could account for the large discrepancy between the modeled bare prompt gamma spectrum and its experimental counterpart in our work.

5.10 Conclusion

The experimental method eliminated geometry-related spectral anomalies and reduced dead time within the detector. The modeled prompt gamma spectra share the same general characteristic shape as their experimental counterparts. Discrepancies between the modeled prompt gamma spectra and the experimental prompt gamma spectra are likely due to short term decay following the reactor's shutdown.

A more robust validation of the modeled prompt gamma spectrum will require additional measurements and models to account for these short-term decay gamma rays. Additional steps that would improve the quality of such a validation would be to increase the distance from the reactor to the detector, use a larger detector to increase the counting efficiency of high-energy gamma rays, and evaluate the reactor with a fresher load of fuel or after an extended shutdown period.

The tungsten sheath technique used in this evaluation could be used for more than reducing dead time and providing multiple points of comparison. By building a response function library with a set of these sheaths, a spectral unfolding algorithm could provide information about high-energy flux environments using small detectors that are inefficient at capturing high-energy gamma rays by themselves.

Acknowledgements

The authors would like to thank the Defense Threat Reduction Agency for its sponsorship and active support of this research and the White Sands Missile Range Fast Burst Reactor staff for their help and professionalism.

VI. Radiation Protection Factors with the Fission Spectrum of a Nuclear Weapon

This chapter describes work towards the verification and validation of MCNP6 for producing RPFs using sources with a fission spectrum from a bare, un-moderated metal uranium reactor and a fission-only nuclear weapon, as well as a comparison of different RPF calculation methods. The fission spectrum introduces three additional challenges for validation. First, fission energy distributions of neutrons and gamma rays make modeling more complicated than sources with discrete energies. Second, experimental fission sources are difficult to characterize as gamma ray emitters, since their emission spectra are a function of both ongoing fission activity and decay radiation from the daughter products of past fission activity, and isolating prompt gamma emissions of fission from decay radiation experimentally requires controlling these confounding variables experimentally. Finally, calculating RPFs from a fission source at distances appropriate for a nuclear weapon requires large-scale simulations. This chapter describes three efforts to mitigate these difficulties and the results of these efforts.

6.1 Gamma Protection Factor Validation Study

As discussed in Chapter 2, a GPF is a unit-less ratio of the dose (D) or dose rate ($\dot{D}$) in a free-field (FF) measurement to a measurement taken within a shielding enclosure (SH) in an otherwise identical radiation field. We will use dose rate as in Equation 13, taken from the Army's RPF evaluation of the M113 armored personnel carrier [82].

$$\boldsymbol{GPF} = \frac{\boldsymbol{D_{FF}}}{\boldsymbol{D_{SH}}} \tag{13}$$

The GPF can be broken into constituent gamma components of prompt gamma (γ) radiation from the reactor, neutron-gamma (nγ) interactions in the environment, and decay radiation from the reactor. Since decay radiation emitted by a reactor can vary significantly depending on the recent operational history of that reactor, and since the most acute source of dose from a nuclear weapon is from its prompt effects, only the components associated with prompt radiation from ongoing fission in the reactor are calculated for the purposes of validation. Thus, for the purposes of this research, these are the only sources of gamma rays included in Equation 14.

$$\boldsymbol{GPF} = \frac{\boldsymbol{D_{\gamma,FF}+D_{n\gamma,FF}}}{\boldsymbol{D_{\gamma,SH}+D_{n\gamma,SH}}} \tag{14}$$

Gamma-based experiments to measure GPF values consisted of several series of measurements with a LaBr (lanthanum bromide) detector in shielded and free-field setups. Each series used bare detector measurements along with measurements taken with the detector surrounded by tungsten sleeves with thicknesses of 1 mm, 2 mm, and 4 mm. These sleeves heavily attenuated lower-energy gamma rays and provided a basis for validating the dose contributions of the higher-energy gamma rays from the reactor.

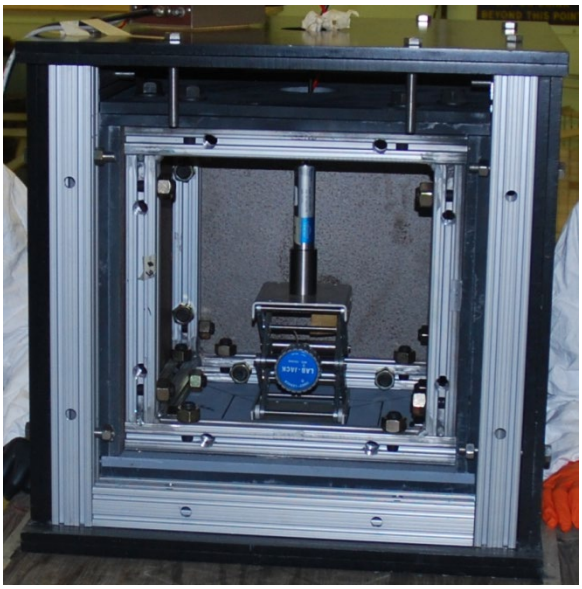

Figure 24. Photograph of the double-layered shielded setup. Shielding panels facing the camera have been removed to show the placement of the detector and its 4mm tungsten sleeve.

The experimental shielded setup reproduced in MCNP6 is shown in Figure 24 for a gamma field measurement. The experiments and models compared three different shielding configurations. The double shield configuration included both the inner and outer steel enclosures, the outer shield configuration included the outer steel enclosure only, and the free field setup had no steel enclosures around the detector. In all three configurations, spectra were measured and simulated with no tungsten sleeve, as well as with 1mm, 2mm, and 4mm tungsten sleeves.

The source was modeled with a prompt gamma emission spectrum produced by White Sands Missile Range (WSMR) models of the FBR. This source term's spectrum had been verified as being similar to experimental observations in previous research [97]. However, this prompt gamma spectrum had not been experimentally validated for producing MCNP-based GPFs, and it did not account for neutron-gamma interactions

outside the FBR, gamma radiation associated with radioactive decay of neutron activation products in the room, or decay gammas from fission fragments and short-lived daughter products within the FBR.

The methodology of this experiment was meant to eliminate as much as was practical of the FBR's gamma spectrum that was not associated with ongoing fission. To this end, each experimental gamma spectrum was produced by this process: the gamma spectrum was measured for 100 seconds with the FBR running at 250 mW, the reactor was shut down, and then the gamma spectrum was then measured for 100 seconds. After normalizing both measurements for time, the shutdown spectrum was subtracted from the 250 mW spectrum.

Some adjustments to the FBR's shutdown procedure were necessary to eliminate changes in spectra associated with the changing geometry of the FBR during normal shutdown. Rather than physically separating the central "safety plug" component from the rest of the FBR, the neutron chain reaction was stopped via manipulation of control rods. The chain reaction took approximately 30 seconds to drop to 1% of its operating neutron flux, at which point the post-shutdown measurement began. The time interval between the initiation of reactor shutdown and the end of the subsequent shutdown spectrum measurement was approximately 130 seconds.

In order to validate the ability of MCNP6 to produce reliable GPF estimates, an F8 pulse-height tally recorded the energy deposited by photon interactions within the simulated detector. Binned by energy, the simulated spectra were compared to experimental measurements. Representations of dose were calculated for both the resulting

experimental spectra and the modeled spectra by multiplying bin count by bin energy for both simulation and experiment in Equation 15.

$$\boldsymbol{Dose} = \frac{\sum_{n=min}^{n=max} \boldsymbol{E_n} \times \boldsymbol{Count_n}}{\boldsymbol{mass_{target}}} \quad (15)$$

In Equation 15, E_n is the energy of the nth bin, $Count_n$ is the count for the *nth* bin, and *min* and *max* are minimum and maximum bins for an energy interval selected. In this case, the energy interval selected was between 30 keV and 1.5 MeV.

6.2 Gamma Protection Factor Results

The top two plots in Figure 25 shows the results of experiment and simulation. A cursory inspection shows that, for each tungsten sleeve thickness, the GPF increases as the steel enclosure shield thickness increases for both experimental and modeling results, which is consistent with established photon transport theory. However, several discrepancies between modeled and experimental GPFs become apparent with closer inspection and the side-by-side comparison of the bottom plot of Figure 25.

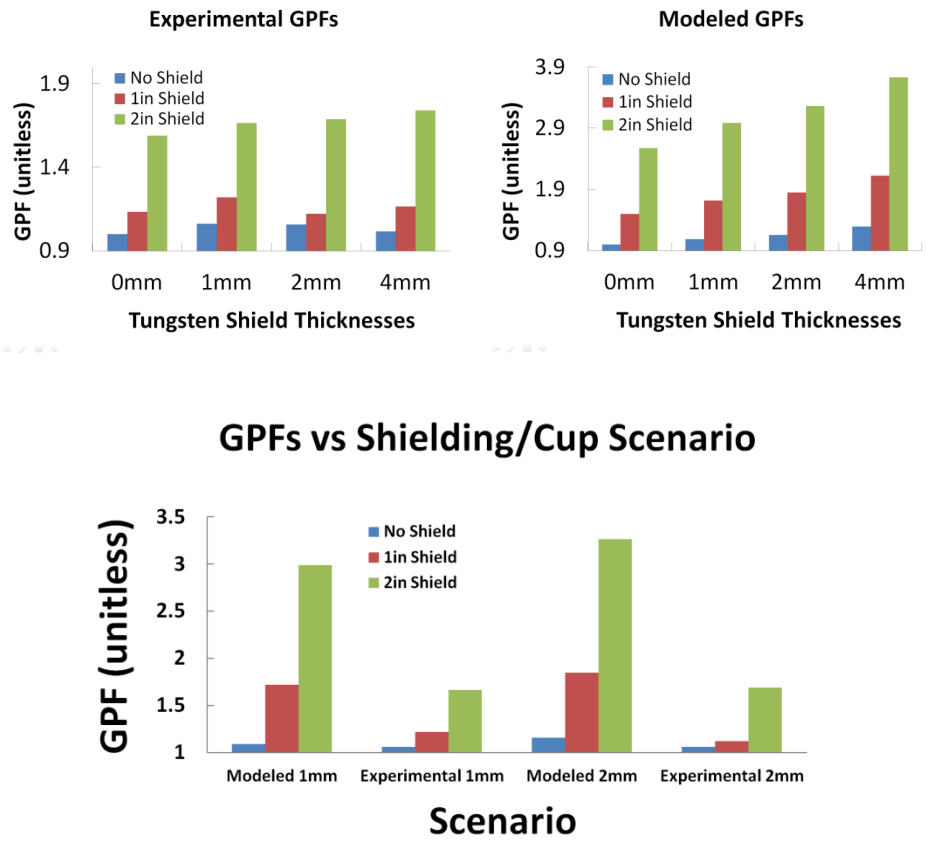

Figure 25. Experimental GPFs (left), modeled GPFs (right). And a side-by-side comparison of the 1mm and 2mm GPFs (below). The red and green bars' shields were outer steel boxes. Statistical error bars in all cases are too small to show at these scales.

The GPF values obtained by modeling were consistently higher than those from experimentation. Although increasing tungsten sleeve thickness also increased the GPF values in the double-shielded experimental results, it did so to a markedly less proportional and less linear degree than in the MCNP models. Furthermore, increasing tungsten sleeve thickness did not consistently increase the GPF value in the experimental results of the unshielded and outer-shielded experimental results. These discrepancies are consistent with discrepancies with measured vs. modeled dose deposition spectra as shown in Figure 26.

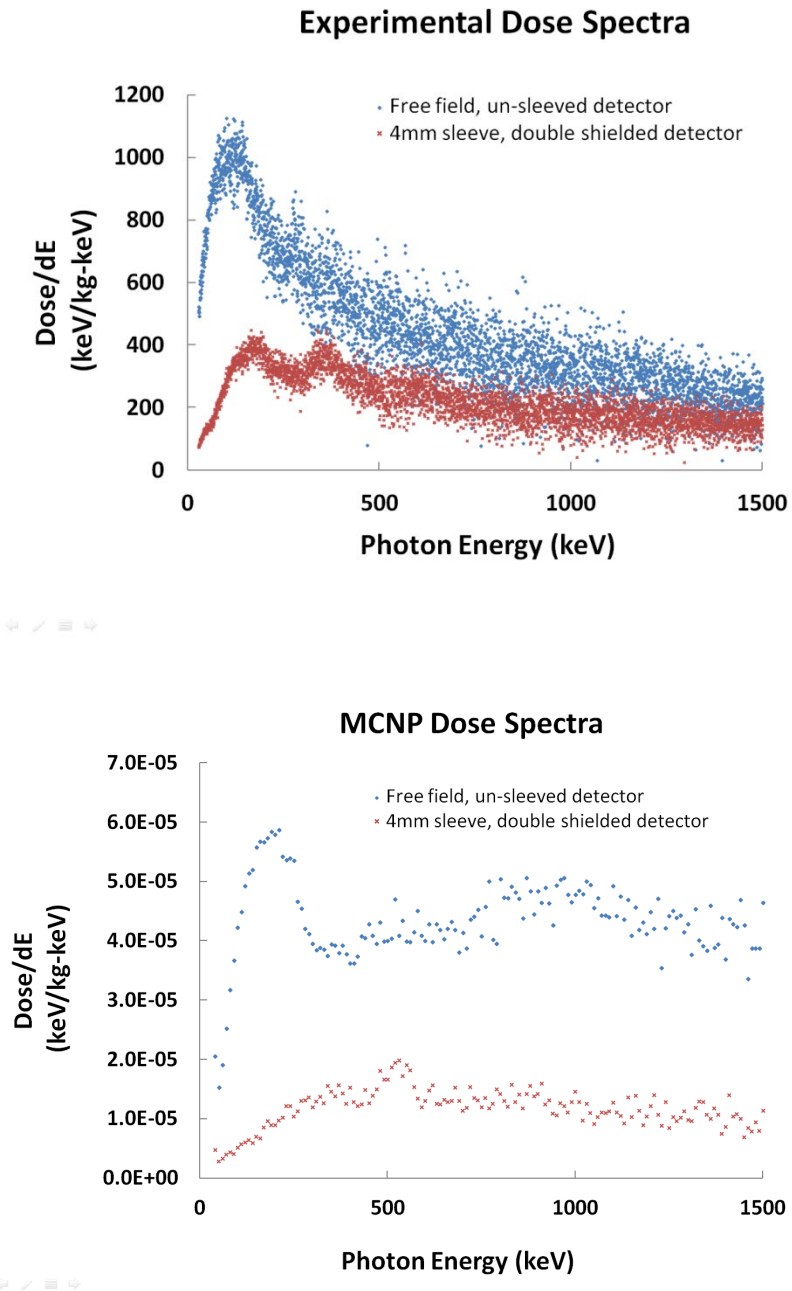

Figure 26. Comparison of unshielded dose spectra between the free field configuration with no sleeve and the double shield configuration with the 4mm sleeve for experiments (above) and MCNP6 (below). Uncertainties for the Experimental Dose Spectra are $2.1 \cdot 10^{2}$ keV/kg-keV and below for the free field, unsleeved detector, and $7.2 \cdot 10^{1}$ keV/kg-keV and below for for the 4mm double sleeved detector. Uncertainties for the MCNP Dose Spectra are $1.1 \cdot 10^{-5}$ keV/kg-keV and below for the free field, unsleeved detector, and $0.5 \cdot 10^{-5}$ keV/kg-keV and below for the 4mm sleeve double shielded detector.

Both the experimental and modeling results indicate significant per-bin attenuation by the double shield and tungsten sleeves. However, the ratio of the modeled dose per unit energy of the free field measurement to the shielded and sleeved dose per unit energy remains steady at approximately 4.5 to 1 for most of the energy range, whereas the same ratio decreases from 3 to 1 at 150 keV to 1.5 to 1 at 1500 keV.

Several alternate modeling approaches were attempted to rule out other contributing factors. In the initial MCNP simulations, electron transport was disabled and MCNP produced subsequent x-ray radiation and dose using the approximation that these occur at the point where the high-energy photon interacts with an electron. Follow-up modeling with electron transport enabled a similar result as in the initial simulation to be produced. Using an alternate prompt gamma modeled spectrum from the Army Pulse Radiation Division Reactor, which was functionally similar to the FBR, also yielded similar results to the modeled spectra presented.

A final modeling attempt to measure the post-fission gamma spectra as a source term in order to simulate the experimental gap between the operating and shutdown spectra was conducted. Adjusting the original simulations' results by subtracting these short-term modeled spectra from the original prompt gamma spectra failed to improve the gap between experimental and observed GPFs.

6.3 Analysis of Discrepancies

The similarity of modeled GPF results with different source spectra and transport modes engaged indicates that the observed discrepancies between the models and experimental observations are more due to experimental conditions than modeling issues.

As stated in the background section, the experimental measurements are an approximation of the radiation field emitted by active fissions in the FBR. While N-gamma contributions were determined to be negligible for LaBr measurements of the FBR in previous research [97], decay gammas from fission fragments, neutron activation products in the chamber, and daughter products are not fully accounted for, as all isotopes with a half-life on the order of a minute or less were not eliminated from the experimental prompt gamma emission spectrum. Since the reactor took approximately 30 seconds to shut down, and the decay radiation from the reactor attenuated over the subsequent 100 second observations, the shutdown spectra was an average of measured radiation between 30 and 130 seconds after the reactor began its shutdown. Measurements of post-fission product radiation from ^{235}U over 128 seconds indicate elevated count rates in the ~0.5 MeV to 1.5 MeV range [95]. Compton scattering other photon interactions in this energy range, and Compton scattering tends to manifest with a small peak-to-Compton edge ratio. Compton interactions in the steel shielding enclosure and tungsten cups will increase the tally rates of scattered photons in detectors. The elevated count rates in the lower energy regions of the sampled interval will tend to decrease the relative dose contribution of the higher-energy prompt gamma spectrum. Additionally, transporting these decay gammas from ^{235}U fission within the FBR is difficult, as this requires detailed information on the FBR's internal structure and its fission density distribution. For security reasons, WSMR does not share its reactor models.

Even with a full model of the FBR and a better accounting of post-fission decay gamma rays and their origination point, the FBR has been an active research reactor for decades, and fully accounting for its decay gamma activity would require a complete

operational history of the reactor and its components, including when each component has been part of the operational reactor, how long each activation took, and the fission rates for each activation. This is not a viable option for further work, as it would require even more technical details on the FBR than an MCNP6 model would provide, and WSMR does not share MCNP6 models of the FBR. In any case the FBR and its associated systems were designed to run in supercritical pulses and steady-state fission rates of up to 8 kW, and its decay radiation is an inconsequential contributor to experiments conducted at those fission rates.

6.4 Summary of GPF Validation Study with the FBR

The experimental and MCNP6 GPFs tend to show the same general trends for varied shield enclosures at all tungsten sleeve thicknesses evaluated. This is consistent with the GPF calculation method and model for a distributed-energy source. However, the inability to experimentally account for short-term decay gammas after shutdown constitutes a confounding variable that cannot be accounted for without detailed information about the design, makeup, and operational history of the reactor, and that information is unavailable. Thus, specific GPF values for shielding geometries against fission sources cannot be validated using this experimental approach.

In order to properly verify MCNP6's ability to model GPFs from a distributed photon source, a different source is required. This could be achieved via a high-energy x-ray source or by a detailed validation study of Compton-scattered radiation from radioisotopes.

6.5 Radiation Protection Factor Methodologies

As discussed in Chapter 2, an RPF is a unit-less ratio meant to express the health benefit of a shielded environment vs. an unshielded environment in an otherwise identical radiation field. However, different health effects require different calculations. Short-term deterministic health effects, such as acute radiation syndrome, are determined by the absorbed dose, which is measured in rads or grays. Long-term stochastic effects, such as cancer, are determined by dose equivalent or equivalent dose, and these are calculated as rems roentgen equivalent man (rem) or sieverts, respectively. These calculations use weighting factors depending on the type and energy of the ionizing particle. In the case of gamma radiation, rad and rem are equivalent, as are gray and sievert. However, in the case of neutron radiation, the energy of incident neutrons determines a weighting factor according to standards published ICRP reports [15].

Thus, an RPF calculation method may require adjustment depending upon the scenario. For example, soldiers subjected to nuclear attack will likely be concerned with short-term effectiveness and survivability far more than long-term cancer risks. Conversely, those same soldiers responding to a radiological emergency that doesn't require immediate lifesaving actions are likely to be primarily concerned with long-term cancer risks. If RPFs for a given radiation field vary to a degree that could affect operational decisions depending on the use of absorbed dose units vs. equivalent dose units, than any product that communicates such RPFs should explain this difference.

While there is no difference between the absorbed gamma dose and its equivalent dose, there are multiple modeling approaches that may result in different calculated RPF values. MCNP6 has the ability to model direct dose depositions in a given object using a

pulse height tally [78]. When a simulated gamma ray interacts in the tallied cell, the randomly sampled interaction energy is tallied within the energy bin with which it is associated. With sufficient counting statistics in enough energy bins, MCNP6 can approximate the spectrum of gamma energy deposited in the object, which can later be summed into an absorbed dose normalized to the number of source particles in a given simulation [78]. This approach offers the benefit of simulating photon interactions in a detector which can be directly compared to a spectrometer.

An alternate approach for calculating gamma dose is to tally all simulated gamma rays crossing into a cell of interest. Using an exposure-dose conversion calculation for each energy bin and summing the result produces a dose normalized to the number of simulated particles. While this result cannot be experimentally validated by spectroscopic measurements, it offers two key benefits. First, it is more computationally efficient to model, since all gamma rays that cross into the cell of interest get tallied. Second, it approximates the dose a human being might absorb when exposed to the radiation field being simulated using the same assumptions of the proportionality of flux and dose as the widely-used 6CEN formula [15].

One additional concern for computing gamma doses for RPF evaluations is selecting an appropriate cell to tally. If a single RPF is to consider both neutrons and gamma rays in a way that can be experimentally validated, then both neutron and gamma simulations should reflect their experimental counterparts and will therefore tally gamma rays and neutrons in cells of different sizes and compositions. If no experimental validation is necessary, then both simulations can tally neutron and gamma radiation into a common cell geometry and composition. If tally cells yield markedly different RPF values due to

different sizes and compositions, then experimental validations of RPFs that use detectors of different sizes and compositions are less likely to adequately model doses from different radiation types and subsequent RPF values.

Procedure

In order to evaluate these considerations, a series of four shielding scenarios were modeled using neutron and prompt gamma spectra from the Fast Burst Reactor (FBR) of White Sands Missile Range. In all cases, the centroid of the shielding enclosure and/or radiation detector was 8 feet from the operating reactor. The first was a free field simulation of the radiation field. The second was a field within a 2 ft x 2 ft x 2ft cubic steel enclosure with a thickness of 1 in. The third replaced a ½ in thickness of the steel with a layer of polyethylene and aluminum. The fourth used the 1 in steel box and added an additional 18 inch x 18 inch x 18 inch steel box inside the original. All neutron simulations tallied neutrons entering a 12 inch diameter sphere of air about the center point of the boxes. Gamma simulation tallies were centered about the center of the boxes and either simulated a 12 inch polyethylene sphere, a 12 inch air sphere, or a 0.75 inch x 2 inch LaBr scintillation crystal.

Gamma doses were calculated from pulse-height tallies by multiplying each bin's energy by the number of interactions tallied at that energy. These products are then summed to produce a value proportionate to gamma dose as shown in Equation 16:

$$\boldsymbol{Dose} = \frac{\sum_{n=min}^{n=max} \boldsymbol{E_n \times Count_n}}{\boldsymbol{mass_{target}}}, \quad (16)$$

where E_n is the energy of gamma rays tallied in the *nth* bin and $Count_n$ is the number of gamma rays tallied in the nth bin. While an actual dose calculation normally includes the mass of the object absorbing this energy, this mass divides out in GPF calculations, and is therefore irrelevant.

Gamma doses were also calculated with an adaptation of the 6CEN approximation for calculating gamma doses as a summation of photon energy, photon fluence for each photon energy, and spherical divergence as a function of distance from a source. Since the distance does not vary for the purposes of GPF calculation, a 6CEN-based approximation of GPF can be calculated using flux data as an input to Equation 16 rather than pulse-height tally data. An alternative to a 6CEN fluence-to-dose calculation is to incorporate NIST data for a target of interest such as human tissue [15]. The resulting Equation 17 is similar to Equation 16 with a fluence-to-dose calculation for each bin,

$$\boldsymbol{Dose} = \frac{\frac{\sum_{n=min}^{n=max} \boldsymbol{E_n \times Count_n} \frac{\boldsymbol{\mu_{en}}}{\boldsymbol{\rho}}}{\boldsymbol{4\pi r^2}}}{\boldsymbol{mass_{target}}}, \quad (17)$$

where $\frac{\mu_{en}}{\rho}$ is the mass energy absorption coefficient divided by the density of the target material. Since this investigation is comparing dose ratios for scenarios in which the distance between source and detector is identical, neither the $4\pi r^2$ term nor the density have any effect upon the resulting RPF, as they are identical in the shielded and free field conditions.

Neutron stochastic dose calculations apply a log-log interpolation of fluence-to-dose and fluence-to-equivalent-dose to modeled neutron flux spectra according to Equation 18,

$$\boldsymbol{Dose} = \frac{\sum_{n=min}^{n=max} \boldsymbol{E_n \times Count_n \times w_r}}{\boldsymbol{mass_{target}}}, \tag{18}$$

where w_r is a quality factor that converts the dose in rads or grays deposited by neutrons of the nth energy bin into a stochastic dose equivalent or equivalent dose of rem or sieverts. This w_r factor varied between 5 and 20 in both ICRP 103 and NCRP 116 at the same energies in both standards [62, 98], so using either standard was unlikely to yield a significant difference in predicted stochastic risks. However, the decision of whether or not to include w_r in the calculation may have a significant effect on neutron doses and the overall RPF in a nuclear attack scenario in which a high fluence of neutrons is expected. Similar to earlier calculations, this is not a true dose calculation, as it omits the mass of the detector or target mass. Since this mass does not change, and since RPFs are ratios of dose, the mass divides out and is therefore irrelevant for the purposes of computing RPFs. Thus, the value computed is proportionate to the equivalent dose, and that is sufficient for the purposes of this research.

Once doses per energy bin and dose equivalencies per energy bin from neutron and gamma fluences were computed for each shielding configuration and calculation scheme, they were summed. The combined unshielded dose values were then divided by their corresponding shielded dose values, producing combined radiation protection factors.

6.6 Gamma Modeling Results

Figure 27 shows the GPFs produced for each simulated shielding scenario and its respective dose calculation scheme. Flux-based calculations consistently yielded higher GPFs than their pulse-height-tally equivalents, and this discrepancy was particularly large for the pulse-height tally of the small detector. Flux-based GPF calculations showed a slight increase (less than 2% of overall GPF) between the small $LaBr_3$ scintillator and the much larger Bonner Ball.

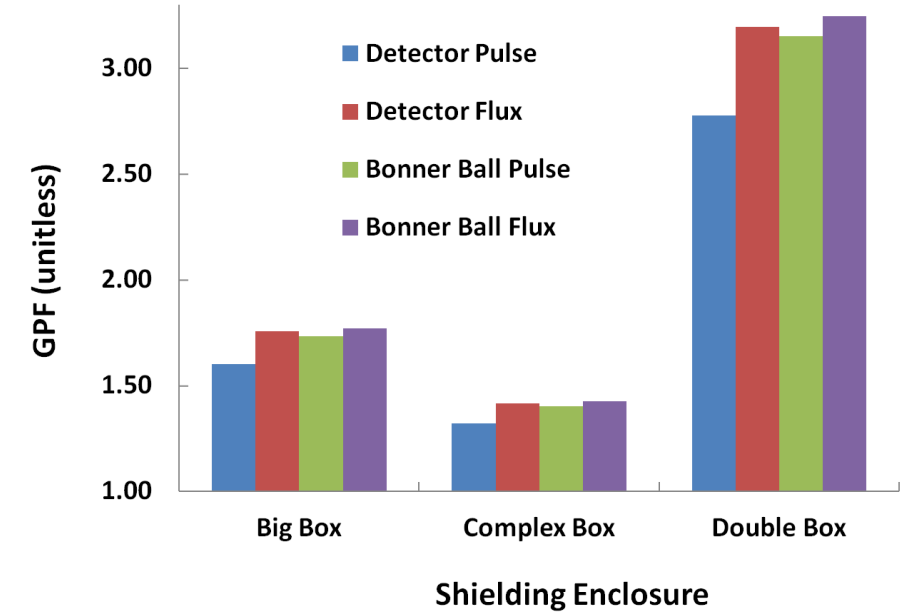

Figure 27. GPFs based on pulse and flux calculations for simulations of a LaBr3 scintillator and a Bonner ball. Due to the large number of summed bins, the uncertainties for these results are ±0.001, too small to resolve error bars.

The consistently lower GPF for the pulse-height tallied $LaBR_3$ simulations is consistent with its small size. Higher-energy photons passing through the smaller detector

are more likely to either not interact at all, or scatter out of the detector without depositing their full energies than in a larger detector, where full-energy depositions are more likely.

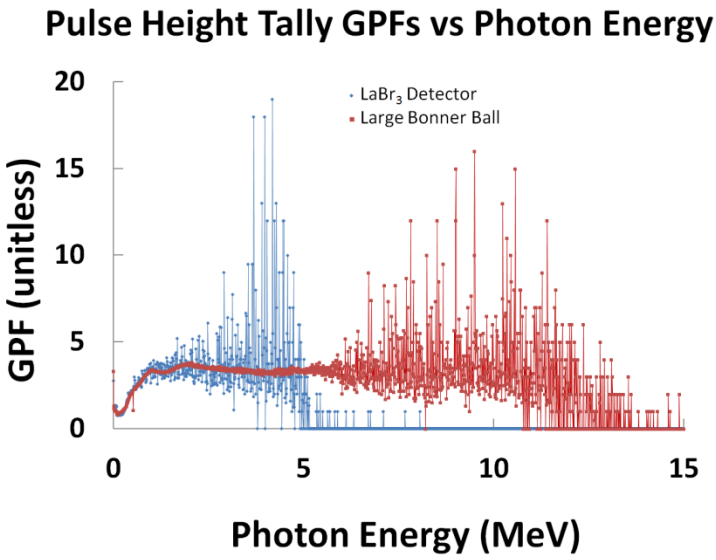

Figure 28. GPFs calculated from MCNP6 pulse-height tallies for the LaBr3 detector (blue) and the Bonner ball (red) in the double-shield scenario. Uncertainties per bin are proportionate to the visual fluctuations in these GPFs per bin, approaching a standard error of 1 as the energy rises above 3 MeV for the $LaBr_3$ detector and 6 MeV for the large Bonner Ball.

Figure 28 shows that the LaBr3 detector was incapable of detecting protection provided by the shielding geometries above 5 MeV, and the variance above 2 MeV is consistent with a lower detector efficiency to be expected from its small size. The larger and heavier Bonner Ball could detect protection provided up to approximately 13 MeV gammas, with much tighter variances than the smaller LaBr detector up to 6 MeV. While these higher-energy photons constitute a small minority of the output of the FBR, their presence drove the GPF up for the larger detector.

Neutron simulation results yielded similar NPFs for both deterministic and stochastic calculation methods as shown in Figure 29 (See Table 1 in Chapter 1 for a

discussion of deterministic and stochastic radiation health effects). However, the stochastic methods of calculation consistently yielded higher NPFs than deterministic methods. This gap was smaller for the 1-inch thick steel big box simulation and larger for the complex box and the 2-inch thick steel box (double box) simulations. This larger gap for thicker shielding suggests that vehicles with heavy armor and higher RPFs may have a wider divergence between RPFs calculated by deterministic vs stochastic methods.

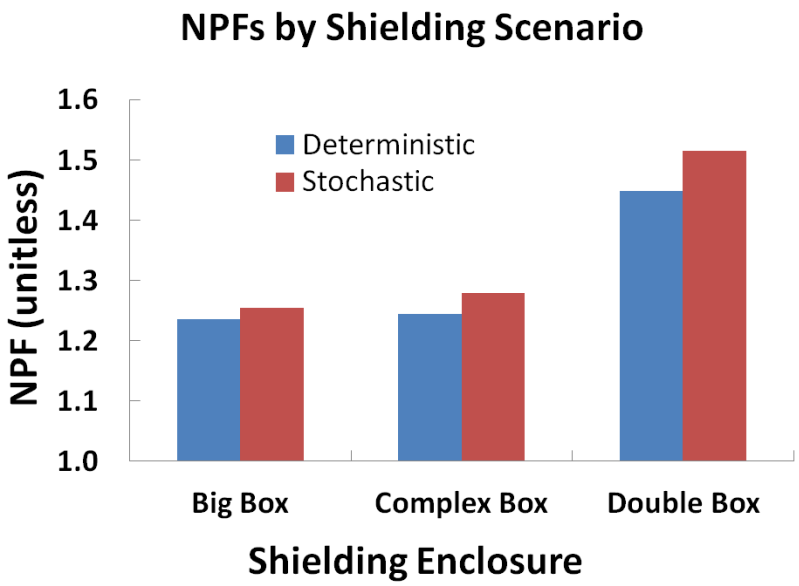

Figure 29. NPFs calculated by deterministic methods (blue) and stochastic methods (red) for three shielding scenarios. Due to the large number of summed bins, the uncertainties for these results are less than ±0.002 and too small to resolve error bars.

Comparing NPFs per bin is not useful as with the GPF comparison, since the difference between the two is defined by an energy bin-specific weighting factor. Thus, the NPFs on a per-bin basis are effectively identical. Instead, it is useful to consider the effect

of the overall spectral shape of a shielded and unshielded neutron flux spectrum and its resulting NPF per bin, as shown in Figure 30.

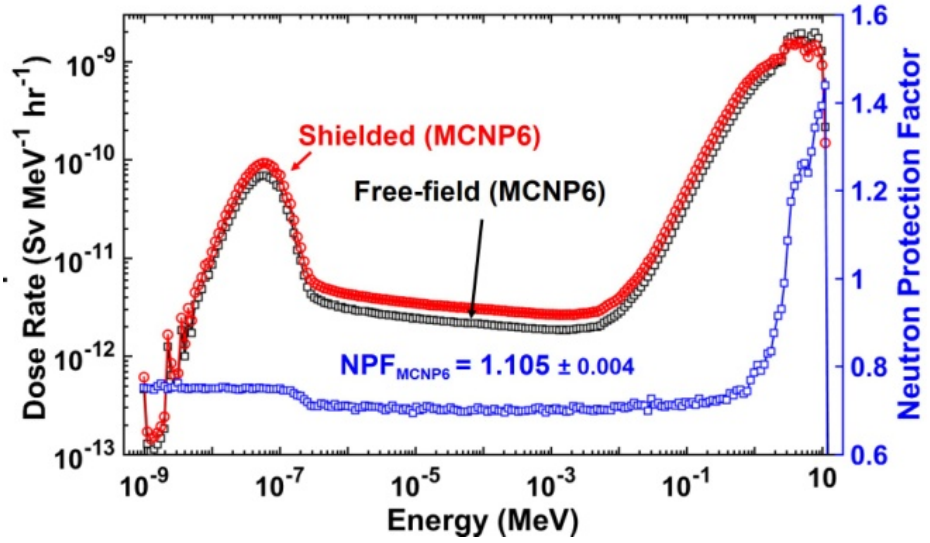

Figure 30. The neutron equivalent dose for free-field and shielded cases from Chapter 4. The neutron protection factor (right axis) shows that presence of the shield actually increases dose for energies lower than ~1 MeV. Standard errors are included for all data but are smaller than the data points displayed. Standard errors are included for all data but are smaller than the data points displayed.

Since shielding materials tend to moderate fast neutrons more often than absorbing them outright, they also tend to reduce their w_r's. As Figure 30 demonstrates, the NPF per bin in a shielding scenario rises above one for neutron energies above 1 MeV but drops slightly below one for neutron energies under 1 MeV. Since the dose rate per bin at fast neutron energies is two orders of magnitude higher than at thermal energies, this increases NPFs calculated via stochastic methods.

6.7 Analysis and Discussion

In considering how to evaluate an RPF, several priorities should be considered. Safety-conscious investigators will likely have an understandable tendency to err on the conservative side of their estimated RPFs, which would indicate using lower-yielding methods. The downside of such an approach is that this may lead risk managers to overestimate the impact of radiation vs. other risks.

Another sensible concern is to avoid relying exclusively on simulations and validate RPF data with calibrated radiation measurements. Choosing to model a detector can provide a direct basis for validating MCNP6-derived RPFs. However, the significant differences between a detector and a human body in geometry and materials can create significant differences between RPFs calculated this way and actual RPFs for a human being. If an RPF evaluator were to use the gamma scintillator used in this study as representative of the dose to a human body with a shielding geometry similar to the double box scenario, that would result in a calculated GPF of approximately 2.7, when the true GPF would be closer to 3.2. Furthermore, since neutron and gamma spectroscopy techniques use detectors of different geometries and materials, combining neutron and gamma doses from measurements introduces systemic error.

Although none of the methods used to simulate and calculate gamma and neutron protection factors yielded differences greater than 14%, these simulations demonstrate several consistent trends worthy of consideration in calculating the protection provided by shields to personnel from neutron and gamma radiation. Pulse-height tallies in MCNP6 are a useful basis for validating the program's ability to model gamma radiation transport and shielding, but the detectors used for such validation should be large enough to capture the

full spectrum of gamma rays present in the scenario; in contrast, a flux tally is adequate for evaluating a GPF at the full range of gamma energies that MCNP6 can model. For NPF calculations, deterministic dose calculation methods yield more conservative protection factors than do stochastic calculation methods. Since deterministic methods are most appropriate for scenarios in which acute radiation sickness is the driving concern, they are best suited for emergency responders and military personnel operating on a nuclear battlefield.

6.8 Simulating a Nuclear Attack on an Armored Vehicle

In order to assess MCNP6's ability to simulate a nuclear attack on an armored vehicle, an attempt was made to model the surface burst of a fission bomb against a Stryker vehicle using a series of MCNP6 simulations and a geometry created in SWORD. This attempt used a multi-step methodology to reduce computational requirements. The first step was a series of gamma and neutron simulations transporting the gamma and neutron spectrum of a Fat Man device from a detonation point 1 meter off the ground to a distance of 1400 meters, where a group of annuli tallied the fluxes. The second step was intended to be a series of simulations transporting the radiation into a SWORD-built prototype model of a Stryker Vehicle in MCNP6, but the model used was found to have geometry problems that introduced fatal errors in MCNP6. While future models may resolve this, it was impractical to find and correct these geometry problems.

Methodology

The Fat Man bomb was chosen for this scenario. This bomb was the original plutonium implosion design, tested at Trinity and used against Nagasaki at the end of

World War II. Although there are simpler methods for creating a nuclear bomb, such as a uranium gun-type device, implosion weapons are suitable to more types of nuclear fuel, making them a more appropriate choice for a wide variety of potential nuclear-armed adversaries as a nuclear weapon in tactical or terrorist strikes. The unclassified source spectra of gamma rays and neutrons for the Fat Man bomb came from DTRA [64].

The burst height of 1m is applicable to multiple plausible scenarios: the tactical deployment of an atomic demolition munition against the U.S. military, the clandestine placement of the bomb in a vehicle or small building as a tactical or terrorist strike against U.S. forces, or the deliberate ground burst of a tactical nuclear weapon in order to achieve an area denial effect through the generation of a highly radioactive debris and a downwind fallout hazard. 1400 meters was chosen for this scenario as a distance at which exposed personnel would likely die from acute radiation syndrome, but personnel inside armored vehicles might survive. On flat ground, at this distance, according to Glasstone and Dolan, the dose from such a burst would be 500 Gy [57], a dose at which acute radiation syndrome would cause approximately 50% lethality, but low enough that an RPF of 2 or more would mitigate symptoms, delay symptom onset, and result in the crew's chances of surviving acute radiation syndrome increasing to 95% [99].

The first step of this attempt was to conduct simulations to transport gamma and neutron radiation from the site of the nuclear explosion to the distance of the target vehicle. The MCNP environment for this step consisted of a cylindrical volume of air 400 meters high and 1500 meters in radius atop a concrete cylindrical slab 0.5 meter thick, which simulated the ground. The 400 meter height of the air and 1 meter depth of the concrete were chosen according to the mean free path lengths of 1 MeV gamma rays and neutrons

in air and concrete. The mean free path of 1 MeV photons in dry air at sea level is 89.0 meters, so 400 meters of vertical space provides in excess of four mean free paths in which photons can go up and scatter back down. The mean free path of 1 MeV photons in concrete is 4.45 cm, so 0.5 meters of concrete depth provides more than 10 mean free paths in which photons can go down and scatter back up. A 1973 cyclotron-based measurement of ordinary concrete measured the half-value thickness for fast neutrons at 9.75 cm ± 0.75 cm for ordinary concrete [100]. A half-value layer is the thickness at which the dose rate from the neutron flux is halved, and since a half-value layer includes a variety of neutron interactions including absorption and scattering, a half-value layer will always be equal to or greater than a mean free path. Thus, there are at least five mean free paths of concrete thickness for neutrons from the explosion to transport down and up on their way to the tallying cells. In the 1951 OPERATION GREENHOUSE nuclear weapon tests, fast neutron mean free paths in air were measured as approximately 152 ± 4.5 meters [101]. Thus, the dimensions of the step one simulation transporting gamma and neutron radiation from the site of the nuclear explosion to the 1400 meter target annuli allow for both gamma rays and neutrons to move up and down for multiple mean free paths while moving from the source to annuli that are many mean free paths distant, while eliminating particles that have moved too far up in air or too far down in concrete to have a statistically significant chance of scattering back into the annuli of interest. Figure 31 shows cross sections of the Step 1 simulation geometry.

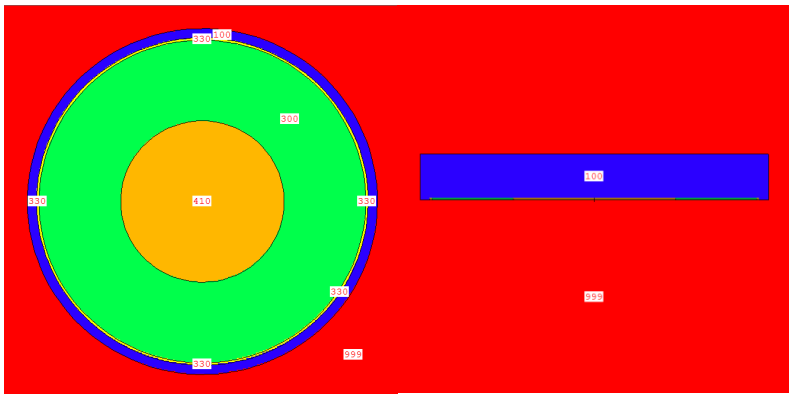

Figure 31. Horizontal and vertical cross sections of the Step 1 simulation geometries. All surfaces are cylinders about the z-axis of the simulation.

Several "killer annuli" dropped the importance of the transported particles to zero, eliminating them from the simulation. These were used to isolate specific components of the incident spectra at the target distance depending on the path of the transported particles, in order to segregate subsequent fluxes into a horizontal flux outward from the explosion and a downward sky-shine flux. Another annulus was created halfway between the simulated bomb and the tallying annuli to have the option to kill particles going straight from the bomb to the tallying annuli with little scattering, but this was found to have little effect on the tallied spectra, and was therefore not used. Using the annulus approximation method described in Chapter 3, MCNP6 transported the source spectra of gamma rays and neutrons to a series of annuli approximately 1400 meters away and tallied them. Figure 32 shows a cross section of the annuli at 1400 meters.

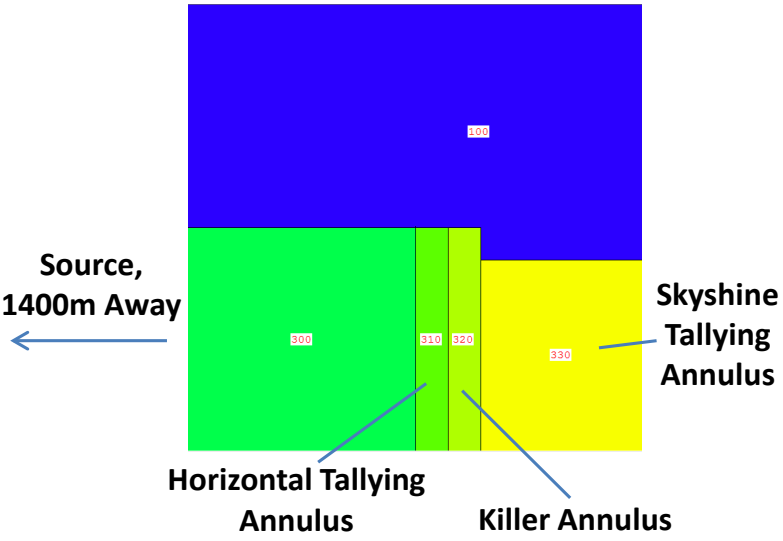

Figure 32. Cross section of tallying annuli and a killer annulus for Step 1 simulations. All cells in this image consist of air. Cell 320 is a killer annulus that eliminates all incident photons from the simulation.

The horizontal tallying annulus was 10 meters tall, but only 1 cm thick; this was meant to minimize the count rate of particles scattering down from above while maximizing incident particles coming horizontally from the direction of the nuclear explosion. Immediately outside the horizontal tallying annulus was a killer annulus that removed all particles entering it from the simulation. A sky-shine tallying annulus was placed just outside the killer annulus and made one cm shorter than the killer annulus in order to prevent horizontal or shallow downward particles from being counted. The sky-shine tallying annulus was made 20 meters thick. The 10 meter height and 20 meter length of these annuli were to be the same as the height and length of the Step 2 simulations. This combination of annuli allowed for a rough approximation of angular-dependent spectra for the target vehicle. Since vehicle armor is thicker to the sides than it is on top, this is a

relevant consideration for shielding and the RPF. These annuli were made to tally the incident spectra of sky-shine and a combination of direct radiation and ground-shine for a ground vehicle at this distance. Figure 33 compares the source photon spectrum with the horizontal and sky-shine tallies.

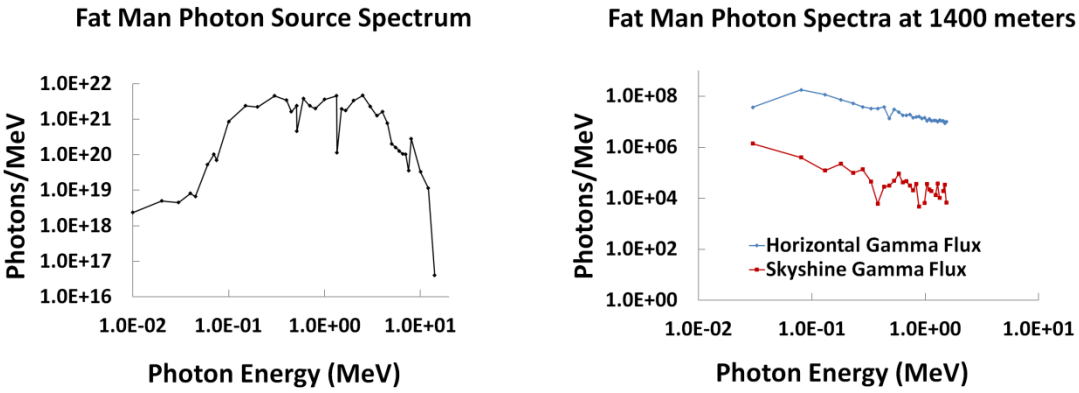

Figure 33. Photon source spectrum for Fat Man (left), recreated from Holmes [102], and tallied photons for horizontal gamma fluxes tallied at 1400 meters (right), normalized to the number of simulated particles, multiplied by the total number of gamma rays emitted by Fat Man according to Holmes, and then adjusted to account for the difference in area between the horizontal and sky-shine tally incident surfaces. Note that the scales are different for these results. Tallied photon counts above 1.5 MeV and below 20 keV were too low to be statistically significant. Uncertainties for the photon flux spectra are $\pm 5 \cdot 10^3$ Photons/MeV.

The gamma ray spectra tallied at 1400 meters has several significant differences from the source spectrum. Whereas the source spectrum shows a large number of gamma rays up to 4 MeV, the tallied spectra showed no statistically significant tallied gamma rays, indicating that photons with these energies have attenuated at this distance. Most remaining photons have energies less than 1 MeV. Additionally, the horizontal gamma flux was a close match to the sky-shine flux below 120 keV, from 400-500 keV, and from 1.5 keV, but the horizontal gamma flux exceeded the sky-shine gamma flux by two orders of magnitude at 200 and 350 keV, and by two to three orders of magnitude from 550 keV to

1 MeV. Thus, the horizontal tallied flux had both more photons per unit area and higher-energy photons per unit area. Most tactical vehicles have their thickest armor oriented to the sides of the occupants, which is fortuitous for these incident-angle-dependent trends.

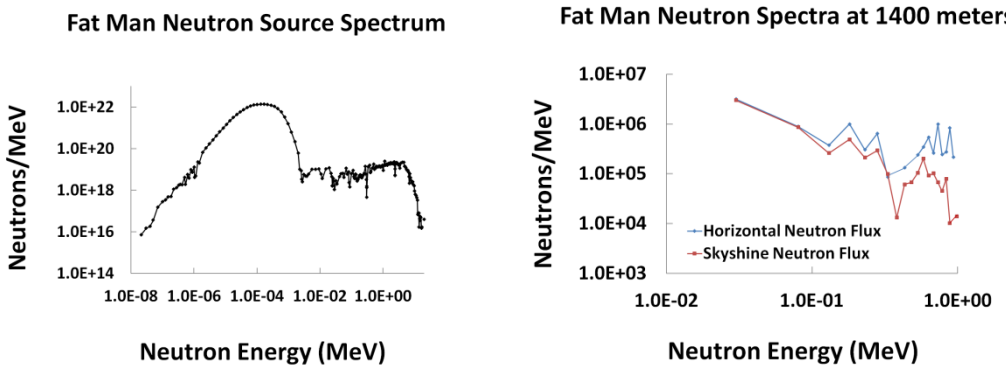

Figure 34. Neutron source spectrum for Fat Man (left), recreated from Holmes [102], and horizontal and skyshine neutron flux spectra tallied at 1400 meters (right), normalized to the number of simulated particles, multiplied by the total number of neutrons rays emitted by Fat Man according to Holmes, and adjusted to account for the difference in area between the horizontal and sky-shine tally incident surfaces. Note the different scales for these results. Tallied neutron counts above 1.0 MeV were too low to be statistically significant. Uncertainties from the neutron flux spectra are $\pm 7 \cdot 10^3$ Neutrons per MeV.

Figure 34 shows that the trends for the step 1 neutron simulations were similar to the trends for the step 1 gamma simulations. The horizontal neutron flux was greater in both incident particles and incident energy than the sky-shine neutron flux, and this was particularly pronounced between 0.5 and 1 MeV and between 150 and 300 keV.

Overall, step 1 simulations took between 6 and 12 hours on a laptop with 8 i7-4700MQ CPU cores running simultaneously, with each simulation transporting 1 billion particles throughout 2.83 billion cubic meters of air and concrete. The ability to transport statistically significant gamma and neutron fluxes through such a large volume to a distance of 1400 meters demonstrates the viability of this approach for evaluating large-scale

nuclear attack. While more computing power and time could help reduce statistical noise and provide improved energy resolution in the tally surfaces, these results were adequate to use as inputs for step 2 simulations of a tactical vehicle.

The Stryker vehicle was chosen for step 2, and a new model, built in SWORD by Naval Research Laboratories, provided a close approximation of the shapes and materials making up this vehicle. A SWORD model was constructed within a box world volume 10 meters tall and 20 meters wide and long. Two thin parallelepiped plates of air were made to serve as source regions for the horizontal and sky-shine fluxes, one on the side of the simulation and one above. A single large sphere within the Stryker was to serve as a tally cell for gamma rays and neutrons. Figure 35 shows the step 2 simulation geometry prior to its export into MCNP6.

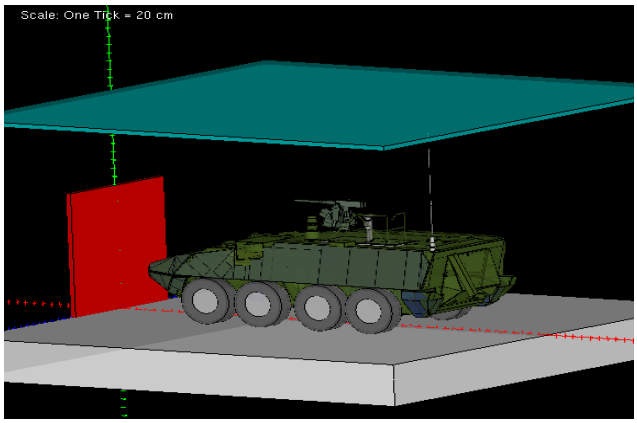

Figure 35. Visualized geometry of the Step 2 simulations in SWORD.

Unfortunately, the model failed in MCNP6 due to intrinsic geometry errors in the Stryker vehicle SWORD model which caused approximately 1 in 1,000 particles to be lost. These losses occurred in areas of the Stryker outside the tallying surface, and with approximately 3,600 lines of code to parse and cross-check for geometry errors, it was

impractically difficult to correct the model in MCNP6 or SWORD. Since these loss rates would have exceeded some of the tallies needed to produce an RPF, these errors prevented step 2 simulations from enabling RPF evaluations of this model.

6.9 Conclusion

This chapter has presented efforts to model RPFs with the fission spectrum of a nuclear weapon. Overall, these efforts had mixed results. GPF validation of the fission spectrum remains elusive due to a source spectrum that yielded modeled GPFs that were from 27% to 106% higher their experimental counterparts. While work described in Chapter 5 successfully measured the gamma spectrum of the FBR, more work is needed to better define this spectrum. This chapter presented an exploration of RPF methodology choices that could affect how a study might present RPF data to military planners and end users of tactical vehicles, but the influence of these factors was determined from surrogate models, not from a model of a tactical vehicle. Finally, the attempt to model a nuclear attack on a tactical vehicle demonstrated the viability of the annulus approximation, but problems with the final model precluded Step 2 evaluations, which made the final RPF evaluation impossible. Thus, the work presented in this chapter, while useful as an iterative step towards RPF evaluations using MCNP6, does not complete the goals of verifying and validating MCNP6 for producing RPFs.

These setbacks also provide insight that may be useful for follow-on work. The methodology used to measure the gamma spectrum of the FBR might be compatible with unfolding algorithms to produce a source spectrum closer to reality. Evaluating a nuclear

strike could well be viable with a newer SWORD Stryker model or a SWORD model of another vehicle.

VII. Conclusions and Recommendations

7.1 Review of Goals and Objectives

The first goal of this dissertation was to create a RPF evaluation method that uses experimentally-validated MCNP6 simulations, a method described in Chapter 3 and accomplished in Chapter 4. As stated in Chapter 1, the supporting objectives of defining NPF and GPF validation with simple surrogates were accomplished in research leading up to this dissertation. Chapter 3 replicated both these processes and combined them into a single RPF value. Chapter 3 also established a procedure for normalizing gamma and neutron dose components in a simulated scenario by using published source ratios and efficiency calculations from experimental measurements, the latter of which was demonstrated in Chapter 4. Chapters 3, 4, and 6 all present procedures for computing doses and the total RPF value, with Chapters 3 and 4 focusing on experimental validation, and Chapter 6 addressing the influence of different simulation and calculation methods upon RPF values.

The second goal was to demonstrate the RPF method on a series of surrogates using a PuBe source and a nuclear reactor. This was accomplished in Chapters 4, 5, and 6, though the demonstration of the RPF method on a reactor in Chapter 6 was not completed due to discrepancies between gamma simulations and measurements. Despite these discrepancies, the data and simulations provided the first-ever close gamma spectrometer measurements of the FBR, and the simulations of FBR experiments provided a basis for model-based RPF method demonstrations on three surrogates.

The final goal, to build a computer model of a Stryker vehicle irradiated by a nuclear weapon spectrum in SWORD and run it in MCNP6, was accomplished, but geometry

problems with the model precluded gathering useful information or performing an RPF evaluation this way.

This dissertation has answered the investigative questions posed in Chapter 1. The steps involved in producing RPF values for different scenarios were examined and discussed throughout the dissertation and specifically demonstrated in Chapters 3 and 6. The reliability of MCNP6 for transporting gamma and neutron radiation and producing RPFs is highly dependent upon accurate source spectra, but is achievable to an enumerated degree through the chi-squared test for neutron spectrum unfolding and the statistical strength and accuracy of gamma ray simulations through the criterion of the 95% confidence interval being within 5% of an experimental RPF value. Chapter 4 presented an example of a validated RPF assessment, while Chapter 6 presented and explored issues that prevented this assessment from fission sources. Chapter 6 also identified and examined additional consideration and techniques necessary to produce a reasonably reliable RPF values for a given scenario within practical limits of computational power and time, specifically with the use of the annulus approximation and multi-step modeling.

7.2 Recommendations

The work verified and validated MCNP6 as a viable tool for computing RPFs with well-defined gamma and neutron emission spectra. The program can do so without the expense and difficulty of setting up analogous experiments. Further RPF validations evaluations in MCNP6 are warranted for nuclear weapon spectra, as well as further validation work to build confidence in the results of such evaluations. Alternate tactical vehicle evaluation using SWORD and MCNP6 could allow for an RPF evaluation. If this

could be done in conjunction with a vehicle irradiation experiment with the FBR, that could enable experimental validation in the most realistic scenario possible short of an atmospheric nuclear weapons test.

For such testing to work, however, further evaluations of the FBR's prompt gamma spectrum are needed. A more-varied array of tungsten sleeves could provide a basis for unfolding a source spectrum that better matches experimental results. Alternately, a larger detector placed at a greater distance, such as during an outdoor test, could provide more useful information for evaluating the FBR's emission spectrum. Another approach could be to take low-power measurements of a fresh, small reactor that uses weapons-grade uranium as its fuel as it comes online for the first time. Should Nasa's Kilopower Program continue in development, testing, and manufacture, these could present opportunities for such a measurement [103]. Whatever the method, a more credible FBR prompt gamma source spectrum could in turn provide a basis for another look at validating GPFs with a fission source without requiring further experimentation. Such a spectrum could also enable RPF experimental validation with a fission source without requiring further experimentation.

While the geometry constructed in SWORD did not ultimately work as intended for this dissertation, the ability to visualize geometry during construction is an invaluable tool. SWORD's utility and interface is far superior to the visual editor program, VISED, that is distributed with MCNP6. The elegance of this pairing is likely to improve as Navy Research Laboratory continues to develop SWORD and SWORD-built models of military vehicles. Alternate tactical vehicle evaluations using SWORD and MCNP6 could allow for an RPF evaluation using models alone. Since un-validated simulations are intrinsically

suspect, this could be done in conjunction with a future vehicle irradiation experiment with the FBR. Such an experimental validation would be the most realistic scenario possible short of an atmospheric nuclear weapons test.

Finally, this RPF work could be applied to aircraft irradiated by terrestrial gamma flash events, solar particle events, and galactic cosmic radiation to evaluate radiation risks to military flight operation. Such an effort is currently under way with a multi-way partnership that includes the United States Air Force School of Aerospace Medicine, the Air Force Institute of Technology, and Los Alamos National Laboratory, but that effort does not yet include the role of the aircraft in the transport of radiation from these events. This would also be closely related to cancer risks in Air Force pilots, the subject of a study currently pending publication for which this dissertation's author is also a contributing author [104], as well as the subject of bill for a DoD-level study currently under consideration by Congress [105].

References

[1] J. H. Gardiner, "Presidential address," in *The Journal of the Roentgen Society*, London, 1916.

[2] R. L. Kathern and P. L. Ziemer, A Brief Sketch in Health Physics: A Backward Glance, New York: Pergamon Press, 1980., 1980.

[3] W. Rollins, "X-Light Kills," *Boston Medical Surgery,* vol. 44, p. 173, 1901.

[4] J. Daniel, "Letter," *Science,* vol. 3, 1896.

[5] W. Markuse, "Dermatitis und Alopecie nach Durchstrahlungsversuchen mit Röntgenstrahlen.," *Deutsche Medizinische Wochenschrift ,* p. 30, 1896.

[6] G. Pfahler, "Protection in Radiology," *American Journal of Roentgenology,* vol. 9, 1922.

[7] G. Kay, "Protection and working conditions in X-ray departments," *British Journal of Radiology,* vol. 1, no. 9, pp. 295-312, 1927.

[8] A. Mutscheller, "Safety standards of protection against X-ray dangers," *Radiology,* vol. 10, p. 466, 1928.

[9] G. Kaye, "The story of protection," *Radiography,* vol. 6, pp. 41-60, 1940.

[10] S. Russ, "The British x-ray and radiation protection committee – a personal retrospect," *BJR,* vol. 26, p. 557, 1953.

[11] A. Banerjee, E. Beckmann, U. Busch, A. Buzzi and A. Thomas, The Story of Radiology, Volume 2, Vienna: European Society of Radiology, 2013.

[12] G. H. Anno, S. J. Baum, H. R. Withers and R. W. Young, "Symptomatology of Acute Radiation Effects in Humans After Exposure to Doses of 0.5-30 Gy," *Health Physics,* 1989.

[13] J. T. Bushberg, "Radiation Exposure and Contamination," University of California, Davis, Davis, 2020.

[14] P. D.L. and R. E., "Solid cancer incidence in atomic bomb survivors: 1958-1998.," Radiation Research, Denver, 2007.

[15] H. Cember, Introduction to Health Physics, 3rd ed, McGraw-Hill, 1996.

[16] E. David, M. Wolfson and V. Fraifeld, "Background radiation impacts human longevity and cancer mortality: reconsidering the linear no-threshold paradigm," *Biogerontology,* vol. 22, no. 1, pp. 189-195, 2021.

[17] E. Bromet, "Mental Health Consequences of the Chernobyl Disaster," *Journal of Radiation Protection,* vol. 32, 2012.

[18] C. N. Davidson, "Armored Vehicle Shielding against Radiation," Army Nuclear and Chemical Agency, Springfield VA, 1979.

[19] J. Barnes, J. Johnson, T. Burns and J. Drischler, "Nuclear Vulnerability of the US M60A1 Tank in an Initial Radiation Environment: MASH Code System Analysis," Oak Ridge National Laboratories, Oak Ridge, 1991.

[20] C. Eisenhauer and L. Spencer, "Approximate Procedure for Calculating Protection From Initial Nuclear Radiation From Weapons," National Bureau of Standards Center for Radiation Research, Gaithersburg, 1988.

[21] J. C. Marquart and J. F. Nellis, "Protection Factors of Combat Systems," *Combating WMD Journal,* vol. Winter/Spring, no. 8, pp. 44-46, 2012.

[22] A. W. Decker, Verification and Validation Report for the Radiation Protection Factor Methodology Using Monte-Carlo n-Particle Code, version 6, Fort Belvoir: Defense Technical Information Center, 2018.

[23] Unknown, "Top500 Supercomputer Database," Top500, 1 June 2021. [Online]. Available: https://www.top500.org/lists/top500/. [Accessed 15 June 2021].

[24] B. Gertz, " Putin's July 4th Message:Russian nuclear-capable bombers intercepted near West Coast in second U.S. air defense zone intrusion in two weeks," 10 July 2015. [Online]. Available: http://freebeacon.com/national-security/putins-july-4th-message/. [Accessed 24 February 2017].

[25] R. Dunham, "Red October redux? John Cornyn demands answers from Pentagon on Russian sub in Gulf of Mexico," 16 August 2012. [Online]. Available: http://blog.chron.com/txpotomac/2012/08/red-october-redux-john-cornyn-demands-answers-from-pentagon-on-russian-sub-in-gulf/. [Accessed 24 February 2017].

[26] L. Kelly, "Russia suspends nuclear agreement, ends uranium research pact with United States," *Reuters,* 5 October 2016.

[27] A. Kramer, "Vladimir Putin Exits Nuclear Security Pact, Citing 'Hostile Actions' by US," *New York Times,* 3 October 2016.

[28] K. Mizokami, "Russia Has Reportedly Deployed Treaty-Breaking Cruise Missiles," *Popular Mechanics,* 14 February 2017.

[29] D. Trump, "@TheRealDonaldTrump," Twitter, 22 December 2016. [Online]. Available: https://twitter.com/realDonaldTrump/status/811977223326625792?ref_src=twsrc%5Etfw. [Accessed 18 February 2017].

[30] J. Mattis, Nuclear Posture Review, Washington, D.C.: Office of the Secretary of Defense, 2018.

[31] M. C. Team, MCNP-A General Monte Carlo N-Particle Transport Code, Version 5, Volume I: Overview and Theory, Los Alamos: Los Alamos National Laboratory, 2003.

[32] B. Bennett, Chernobyl's Legacy: Health, Environmental, and Socio-Economic Impacts", Geneva: World Health Organization, 2005.

[33] E. B. Douple, K. Mabuchi, H. Cullings, D. Preston, K. Kodama, Y. Shimizu, S. Fujiwara and R. Shore, "Long-term Radiation-Related Health Effects in a Unique Human Population: Lessons Learned from the Atomic Bomb Survivors of Hiroshima and Nagasaki," *Disaster Medicine Public Health Preparation,* vol. 5, no. 1, pp. 122-133, 2011.

[34] A. W. Decker, Verification and Validation of Monte Carlo n-Particle Code 6 (MCNP6) with Neutron Protection Factor Measurements of an Iron Box, Air Force Institute of Technology, 2014.

[35] W. J. Erwin, Verification and Validation of Monte Carlo Neutral Particle 6 for Computing Gamma Protection Factors, Air Force Institute of Technology, 2015.

[36] W. Erwin, E. Cazalas and J. McClory, "Development of Radiation Protection Factors with Gamma and Neutron Spectroscopy Using a Plutonium-Beryllium Source," *Journal of Radiation Effects,* vol. 36, no. 1, pp. 66-71, 2018.

[37] J. Hall, S. Ha, R. Prins and A. Decker, "Verification and Validation of MCNP6.1 Gamma Protection Factor Estimates Using an Armored Box and Phantom," *Journal of Radiation Effects, Research and Engineering,* vol. 1, pp. 103-110, 2017.

[38] C. Bouvier and A. Decker, "Effects of Model Fidelity on Gamma Protection Factor Estimates Using Monte Carlo n-Particle Code 6.1," *Countering Weapons of Mass Destruction Journal,* no. 15, pp. 9-12, 2017.

[39] U. S. Strategic Bombing Survey, "The Effects of the Atomic Bombings of Hiroshima and Nagasaki," *Harry S. Truman Presidential Library and Museum,* vol. Truman Papers, no. President's Secretary's File, 1946.

[40] B. E. (1946), "Operation Crossroads: The Effect of the Atomic Bomb on Naval Power," *Bulletin of the Atomic Scientists,* vol. 1, no. 5, p. 1, 1946.

[41] R. Miller, Under the Cloud: The Decades of Nuclear Testing, New York: Two Sixty Press, 1999.

[42] D. P. Affairs, "Operation TEAPOT Fact Sheet," Defense Threat Reduction Agency, Albequerque, 2007.

[43] T. Wimett, *Fast Burst Reactors in the United States of America,* Vienna: International Atomic Energy Agency , 1965.

[44] S. Holinka, "Sun Sets on Sandia Pulsed Reactor," December 2007. [Online]. Available: https://share.sandia.gov/news/resources/releases/2007/reactor.html. [Accessed 15 January 2016].

[45] M. A. Oliver, "Army Pulse Radiation Facility (APRF) Gamma Dose Measurements," US Army Combat Systems Test Activity, Aberdeen Proving Ground, 1993.

[46] S. Riley, *Army Regulation 70-75: Survivability of Army Personnel and Material,* Washington, D.C. : Department of the Army, 2005.

[47] T. M. Flanders and J. L. Meason, "Radiation environment for the White Sands Missile Range Fast Burst Reactor in outdoor operations," in *Proceedings of the Fast Burst Reactor Workshop*, Albuquerque, 1986.

[48] L. Townsend, J. Shinn and J. Wilson, "Interplanetary Crew Exposure Estimates for the August 1972 and October 1989 Solar Particle Events.," *Radiation Research,* vol. 126, no. 1, pp. 108-110., 1991.

[49] P. Spillantinia, M. Casolinob, M. Durantec, R. Mueller-Mellind, G. Reitze, L. Rossif, V. Shurshakovg and M. Sorbih, "Shielding from cosmic radiation for interplanetary missions: Active and passive methods," in *International Cosmic Ray Conference*, 2005.

[50] R. A. Mewaldt, D. A. J., W. R. Binns, G. A. de Nolfo, J. S. George and M. H. Israel, "The Cosmic Ray Radiation Dose in Interplanetary Space Present Day and Worst-Case Evaluations," in *International Cosmic Ray Conference*, 2005.

[51] NASA, "Comparison of Some Doses to Mars Trip Level," NASA, 2012. [Online]. Available: https://www.nasa.gov/mission_pages/msl/multimedia/pia17061.html. [Accessed 16 June 2021].

[52] Z. G. Burson and A. E. Profio, "Structure Shielding in Reactor Accidents," *Health Physics,* 1977.

[53] K. Nagatani, S. Kiribayashi, Y. Okada, K. Otake, K. Yoshida, S. Tadokoro, T. Nishimura, T. Yoshida, E. Koyanagi, M. Fukushima and S. Kawatsuma, "Gamma-ray irradiation test of Electric components of rescue mobile robot Quince," in *IEEE International Symposium on Safety,Security and Rescue Robotics*, Kyoto, 2011.

[54] Krane, Introductory Nuclear Physics, Wiley, 1988.

[55] C. J. Bridgman, Introduction to the Physics of Nuclear Weapons Effects, Virginia: Defense Threat Reduction Agency, 2001.

[56] J. Shultis, Radiation Shielding, La Grange Park: Anerican Nuclear Society, 2000.

[57] S. Glasstone and P. Dolan, The Effects of Nuclear Weapons, Washington, D.C.: The United States Department of Defense and the United States Department of Energy, 1977.

[58] A. Ferrari, M. Pellicioni and M. Pillon, "Fluence to Effective Dose Conversion Coefficients for Neutrons up to 10 TeV," *Radiation Protection Dosimetry,* vol. 71, no. 3, pp. 165-173, 1997.

[59] H. Kluge and K. Weise, "The Neutron Energy Spectrum of a 241Am-Be(Alpha,n) Source and Resulting Mean Fluence to Dose Equivalent Conversion Factors," *Radiation Protection Dosimetry,* vol. 2, no. 2, pp. 85-93, 1982.

[60] A. Ferrari and M. Pelliccioni, "Fluence to Dose Equivalent Conversion Data and Effective Quality Factors for High Energy Neutrons," *Radiation Protection Dosimetry,* vol. 76, no. 4, pp. 215-224, 1998.

[61] ICRP, "ICRP Publication 74: Conversion Coefficients for use in Radiological Protection against External Radiation," Annals of the ICRP, New York, 1996.

[62] ICRP, "Publication 103: The 2007 Recommendations of the International Commission on Radiological Protection," ICRP, Ann., 2007.

[63] ICRU, "ICRU 57: Conversion Coefficients for Use in Radiological Protection Against External Radiation," International Commission on Radiation Units and Measurements, Bethesda, 1998.

[64] DTRA, "DTRA-TR-17-026 Publicly Released Prompt Rad Spectra," Defense Threat Reduction Agency, Annapolis, 2017.

[65] J. Kelly and D. Vehar, "Measurement of neutron spectra in varied environments by the foil-activation method with arbitrary trials," Sandia National Laboratories, Albuquerque, 1987.

[66] W. V. Behrens, "The Effects of Short Duration Neutron Radiation on Semiconductor Devices," Diamond Ordnance Fuze Labs, 1958.

[67] M. Bowling and S. Ader, "The Army Nuclear Survivability Program," US Army Nuclear and Chemical Agency, Ft. Belvoir, 1980.

[68] J. Hubbel and S. Seltzer, *Tables of X-Ray Mass Attenuation Coefficients and Mass Energy-Absorption Coefficients from 1 keV to 20 MeV for Elements Z = 1 to 92 and 48 Additional Substances of Dosimetric Interest.,* National Institute of Standards and Technology, 2016.

[69] C. Eisenhauer, "An Enginnering Method for Calculating Protection Afforded by Structures Against Fallout Radiation," National Bureau of Standards, Washington, D.C., 1964.

[70] A. Chilton, J. Shultis and R. Faw, "Principles of Radiation Shielding," Prentice Hall Inc; , Old Tappan, NJ, 1984.

[71] F. Mynatt, F. Muckenthaler and P. Stevens, "Development of Two-Dimensional Discrete Ordinant Transport Theory for Radiation Shielding," University of Tennessee, Knoxville, 1969.

[72] W. A. Rhoades and F. R. Mynatt, "DOT III two-dimensional discrete ordinates transport code," Oak Ridge National Laboratory, Oak Ridge, 1973.

[73] W. Rhoades and R. Childs, "The TORT three-dimensional discrete ordinates neutron/photon transport code," Oak Ridge National Lab, Oak Ridge, 1987.

[74] D. W. Rogers, "Fifty years of Monte Carlo simulations for medical physics," *Physics in Medicine and Biology,* vol. 51, no. 13, 2006.

[75] W. Rhoades, "Development of a Code System for Determining Radiation Protection of Armored Vehicles (the VCS Code)," Oak Ridge National Laboratory, Oak Ridge, 1974.

[76] W. Rhoads, "VCS, Radiation Protection Factors in Vehicles by Monte-Carlo," Nuclear Energy Agency, 21 November 2001. [Online]. Available: http://www.oecd-nea.org/tools/abstract/detail/ccc-0262/. [Accessed 15 February 2017].

[77] Goldhagen and M. Reginatto, "MAXED, A Computer Code for the Deconvolusion of Multisphere Neutron Spectroscopy Data using the Maximum Entropy Method," Environmental Measurements Laboratory, New York, 1998.

[78] D. B. Pelowitz, *MCNP6 USER'S MANUAL,* Los Alamos: Los Alamos National Security, 2013.

[79] Ludlum, "Model 42-5 Neutron Detector & Ball Cart," March 2015. [Online]. Available: http://ludlums.com/images/stories/data_sheets/M42-5.pdf. [Accessed 27 February 2017].

[80] H. Vega-Carrilloa, E. Manzanares-Acuna, A. Becerra-Ferreiro and A. Carrillo-Nunez, "Neutron and gamma-ray spectra of 239PuBe and 241AmBe," *Applied Radiation and Isotopes,* vol. 57, pp. 167-170, 2002.

[81] Saint-Gobain, "BrilLanCe Scintillation Material," 2004. [Online]. Available: http://www.crystals.saint-gobain.com/sites/imdf.crystals.com/files/documents/brillance380-material-data-sheet_69765.pdf. [Accessed 27 February 2017].

[82] S. Stueker, A. Rainis and R. Schwenk, "M113A1 Armored Personnel Carrier - Initial Radiation Protection Factors," U.S. Army Armament Research and Development Command, Aberdeen Proving Grounds, 1978.

[83] T. Goorley and e. al., "Initial MCNP6 Release Overview," *Nuclear Technology,* vol. 180, no. 1, pp. 298-315, 2012.

[84] M. Reginatto and P. Goldhagen, "MAXED, a Computer Code for Maximum Entropy Deconvolution of Multisphere Neutron Spectrometer Data," *Health Physics,* vol. 77, no. 5, p. 579*583, 1999.

[85] A. Obst, T. Grandy and J. Weil, "Reaction 9Be(α,n)12C from 1.7 to 6.4 MeV," *Physical Review C,* vol. 5, no. 3, 1972.

[86] D. Reilly, N. Ensslin, H. Smith and S. Kreiner, "Passive Nondestructive Assay of Nuclear Materials LA-UR-90-732," Los Alamos, 1991.

[87] R. Lindstrom and R. Fleming, "Dead Time, Pileup, and Accurate Gamma-Ray Spectroscopy," *Radioactivity and Radiochemistry,* vol. 6, no. 2, 1995.

[88] A. Decker, S. McHale, J. M. J.A. Clinton and M. Millett, "Verification and Validation of MCNP6.1 Neutron Protection Factor Estimates Using the WSMR Fast Burst Reactor," *Journal of Radiation Effects, Research and Engineering,* vol. 35, no. 1, pp. 52-58, 2017.

[89] T. Gates, C. Zeigler, C. Bouvier and A. Decker, "Verification and Validation of MCNP6.1 for Gamma Protection Factor Estimates of an Armored Box," *Journal of Radiation Effects, Research and Engineering,* vol. 35, no. 1, pp. 83-90, 2017.

[90] C. Longmire, "On the electromagnetic pulse produced by nuclear explosions," *IEEE Transactions on Antennas and Propagation,* vol. 26, no. 1, pp. 3-13, 1978.

[91] H. J. Longley and C. L. Longmire, "Development of the CHAP EMP code," DNA Report 3150, Dayton, 1972.

[92] F. Tesche and P. R. Barnes, "Development of a new high altitude electromagnetic pulse (HEMP) environment and resulting overhead line responses.," *Electromagnetics,* vol. 8, no. 4, pp. 213-239, 1988.

[93] M. A. Gibson and e. al., "NASA's Kilopower reactor development and the path to higher power missions," in *2017 IEEE Aerospace Conference*, Houston, 2018.

[94] E. Jurney, P. Bendt and T. England, "Informal Report LA-7620-MS: Fission Product Gamma Spectra," IAEA, Vienna, 1979.

[95] R. Drinkwater, "Gamma Radiation from Fission Products AD-777 842," National Technical Information Service, Alexandria, 1974.

[96] G. Rudstam, P. Johansson, O. Tengblad, P. Aagaard and J. Eriksen, "Beta and Gamma Spectra of short-lived fission products," *Atomic Data and Nuclear Tables,* vol. 45, no. 2, 1990.

[97] W. Erwin, "The Gamma Emission Spectrum from the Fast Burst Reactor," *Journal of Radiation Effects,* vol. 37, no. 1, pp. 50-56, 2019.

[98] NCRP, "Report No. 116: Limitation of Exposure to Ionizing Radiation," National Council on Radiation Protection, Bethesda, 1994.

[99] J. T. Bushberg, "Radiation Exposure and Contamination," Merck Manual, Davis, 2020.

[100] K. W. H.M. Butler, "Half-Value Thickness Measurements of Ordinary Concrete for Neutrons from Cyclotron Targets," Atomic Energy Commission, Oak Ridge, 1973.

[101] J. C. Allred, D. D. Phillips and L. Rosen, "Scientific Director's Report of Atomic Weapon Tests at Eniwetok, 1951," Los Alamos Scientific Laboratory, Los Alamos, 1951, declassified 1999.

[102] R. L. Holmes and S. W. White, "Output of Fat Man and Little Boy Devices. LA-UR-13-26113.," Los Alamos National Laboratory, Los Alamos, 2013.

[103] NASA, "The Fission System Gateway to Abundant Power for Exploration," NASAfacts, 2018. [Online]. Available: https://www.nasa.gov/sites/default/files/atoms/files/ns_kilopower_fs_180111.pdf.. [Accessed 15 November 2019].

[104] B. J. Webber, C. D. Tacke, G. G. Wolff, A. E. Rutherford, W. J. Erwin, J. D. Escobar, A. A. Simon, B. H. Reed, J. G. Whitaker, K. J. Gambino-Shirley and D. M. Steuver, "Cancer Incidence and Mortality among Fighter Pilots in the United States Air Force," *International Journal of Cancer,* 2021.

[105] D. Feinstein, *Military Aviators Cancer Incidence Study Act,* Washington: United States Senate, 2020.

[106] R. Griffith and J. Palfalvi, Compendium of neutron spectra and detector responses for radiation protection purposes, Vienna: International Atomic Energy Agency (IAEA), 1990.

[107] G. F. Knoll, Radiation Detection and Measurement, 4th edition, New York: Wiley, 2010.

[108] J. Kelly, "Neutron Spectrum Adjustment with SANDII Using Arbitrary Trial Functions," *Reactor Dosimetry: Methods, Applications, and Standardization,* pp. 460-468, 1989.

[109] J. Meason, H. Wright, J. Hogan and J. Harvey, "The Neutron Spectral Distribution from a Godiva Type Critical Assembly," *IEEE Transactions on Nuclear Science,* vol. 22, no. 6, pp. 2330 - 2335, 1975.

[110] A. W. Decker, "Verification and Validation Report for the Radiation Protection Factor Methodology using Monte-Carlo n-Partical Code, version 6 (DTRA-TR-18-71)," Defense Threat Reduction Agency, Fort Belvoir, 2018.

[111] P. C. Fisher and L. B. Engle, "Delayed Gammas from Fast-Neutron Fission of Th 232, U 233, U 235, U 238, and Pu 239," *Physical Review,* vol. 134, no. B796, 1964.

[112] V. V. Verbinski, N. A. Lurie and V. C. Rogers, "Threshold-Foil Measurements of Reactor Neutron Spectra for Radiation Damage Applications," *Nuclear Science and Engineering,* vol. 65, no. 2, pp. 316-330, 1978.

[113] J. Vitorellia, A. Silva, V. Crispim, E. d. Fonseca and W. Pereira, "Monte Carlo simulation of response function for a NaI(Tl) detector for gamma rays from 241Am/Be source," *Applied Radiation and Isotopes,* vol. 62, no. 4, pp. 619-622, 2005.

[114] B. Kamboj and M. Shahani, "Precise measurement of the gamma to neutron ratio of an Am-α-Be neutron source using an improved manganese bath technique," *Nuclear Instruments and Methods in Physics Research Section A: Accelerators, Spectrometers, Detectors and Associated Equipment,* vol. 244, no. 3, pp. 513-515, 1986.

[115] D. Drake, J. Hopkins and J. Martin, "The use of Pu α Be as a calibrated gamma ray source," *Nuclear Instruments and Methods,* no. 3, pp. 349-350, 1968.

REPORT DOCUMENTATION PAGE

Form Approved
OMB No. 0704-0188

1. REPORT DATE *(DD-MM-YYYY)*	2. REPORT TYPE	3. DATES COVERED *(From - To)*
16-09-2021	Ph.D. Dissertation	Mar 2017 - Sep 2021

4. TITLE AND SUBTITLE
Verification and Validation of Radiation Protection Factors from Monte Carlo Simulations

5a. CONTRACT NUMBER

5b. GRANT NUMBER

5c. PROGRAM ELEMENT NUMBER

6. AUTHOR(S)
Erwin, William J., Major, USAR

5d. PROJECT NUMBER

5e. TASK NUMBER

5f. WORK UNIT NUMBER

7. PERFORMING ORGANIZATION NAME(S) AND ADDRESS(ES)

Air Force Institute of Technology
Graduate School of Engineering and Management (AFIT/EN)
2950 Hobson Way
Wright-Patterson AFB OH 45433-7765

8. PERFORMING ORGANIZATION REPORT NUMBER
AFIT-ENP-DS-21-S-027

9. SPONSORING / MONITORING AGENCY NAME(S) AND ADDRESS(ES)
Defense Threat Reduction Agency
Major Joshua Frey
8725 John J. Kingman Rd
Ft. Belvoir, VA 22060
joshua.frey@westpoint.edu

10. SPONSOR/MONITOR'S ACRONYM(S)
DTRA

11. SPONSOR/MONITOR'S REPORT NUMBER(S)

12. DISTRIBUTION / AVAILABILITY STATEMENT
Distribution Statement A. Approved for Public Release; Distribution Unlimited

13. SUPPLEMENTARY NOTES

14. ABSTRACT
This dissertation describes the verification and validation of methods for producing radiation protection factors (RPFs) using experiments and Monte Carlo N-Particle 6 (MCNP6) simulations. RPF validation of a steel enclosure using a plutonium-beryllium source produced a validated RPF of 1.187 ± 0.003, with statistically significant agreement between neutron MCNP6 models and experiments and a gamma protection factor (GPF) with statistically significant agreement to the measured GPF with a 95% confidence interval. Efforts to validate more complex enclosures using the Fast Burst Reactor (FBR) yielded the first-ever direct measurements of this reactor's prompt gamma emission spectrum and revealed irreconcilable differences between the FBR facility-provided source spectrum and spectrometer measurements, resulting in modeled GPFs 27% to 106% higher than experimental GPFs. The use of a tallying annulus reduced the variance in simulations of the FBR's projected radiation field by three orders of magnitude. Annulus-based tallying enabled the demonstration of a nuclear weapon-like irradiation of a target at 1400 meters, yielding statistically significant gamma and neutron flux spectra in 36 hours using a laptop computer with an i7-4700MQ processor. The effects of different simulation and calculation methods on RPFs are examined and discussed, along with recommendations and lessons learned for future work.

15. SUBJECT TERMS
Radiation Transport, Dosimetry, Protection, MCNP6, Radiation Protection Factor

16. SECURITY CLASSIFICATION OF: UNCLASSIFIED			17. LIMITATION OF ABSTRACT	18. NUMBER OF PAGES	19a. NAME OF RESPONSIBLE PERSON
a. REPORT	b. ABSTRACT	c. THIS PAGE	UU	134	Dr. John McClory
U	U	U			19b. TELEPHONE NUMBER *(include area code)* (937) 255-3636 x7308